Journal of Energy Storage 68 (2023) 107846

Contents lists available at ScienceDirect

Journal of Energy Storage

journal homepage: www.elsevier.com/locate/est

Research papers

# A comprehensive experimental and modelling approach for the evaluation of cross-over fluxes in Vanadium Redox Flow Battery

Marco Cecchetti *, Francesco Toja, Andrea Casalegno, Matteo Zago

*Politecnico di Milano, Department of Energy, Via Lambruschini 4, 20156 Milano, Italy*

ARTICLE INFO

*Keywords:*
Vanadium cross-over
Electrolyte imbalance
Reference electrodes
Model
Vanadium redox flow battery

ABSTRACT

Vanadium cross-over is a critical issue in Vanadium Redox Flow Battery consisting in a complex interplay of different mechanisms of which a complete comprehension has not been reached yet. Due to the complexity of the involved phenomena, several models have been developed in literature to investigate vanadium cross-over. However, the conventional approaches for model calibration present a limited set of experiments for the validation preventing a complete understanding of cross-over phenomena. In this work a new and comprehensive approach is proposed. It is based on charge-discharge cycles with fixed exchanged capacity, able to isolate the capacity loss induced by cross-over fluxes, and on the measure of the self-discharge of the single electrolyte solutions by exploiting through-plate reference electrodes. Moreover, a 1D physically-based model of the operation of the battery is developed and calibrated on the data of electrolyte imbalance during charge-discharge cycles at three different current densities to obtain model parameters able to accurately describe the involved physics in different operating conditions. The model is then exploited to investigate the main vanadium transport mechanisms through the membrane and to evaluate the influence of the current density on the vanadium cross-over fluxes, net vanadium transport and self-discharge rate of the electrolyte.

## 1. Introduction

The rapid growth of the penetration of energy from renewable sources in the energy markets due to specific energy policies aimed at the reduction of carbon emissions requires efficient and cost-effective energy storage systems [1–4]. The growth of energy storage capacity requirement for load-shifting, peak shaving and grid stability applications is predicted to be met with electrochemical energy storage, in particular with batteries [5]. As a matter of fact, the global installed capacity of batteries grew by 60 % in 2021 from 10 GW to 16 GW and it is predicted to grow up to 680 GW by 2030 in the Net Zero Emissions scenario [5]. In this context, lithium-ion batteries are the leading technology, however safety issues, rising prices and uncertainties in the supply of raw materials highlight the need for alternative technologies [5–7].

High efficiency, decoupled energy and power, long cycle life, high flexibility and low response time make Vanadium Redox Flow Battery (VRFB) a promising technology for stationary energy storage. Indeed, the market size for flow batteries has been forecasted to be the 11.5 % of the emerging global battery market in 2030 with a value around 2 billion USD, increasing by +300 % with respect to the size in 2021 (~0.5 billion USD) [8]. However different technical issues hinder the competitiveness, among which vanadium cross-over is one of the most important. Cross-over is the undesired permeation of vanadium species from one side of the battery to the other due to the employment of not-ideally selective ionic separators [9,10]. Although vanadium cross-over is completely reversible by electrolyte remixing [11], it causes the self-discharge of both electrolytes according to the reactions (1.1)–(1.4) [12], leading to battery capacity reduction during the operation and electrolyte solutions imbalance, negatively affecting the performance of the battery [9,10].

$$VO_2^+ + 2V^{2+} + 4H^+ \rightarrow 3V^{3+} + 2H_2O \quad (1.1)$$

$$VO^{2+} + V^{2+} + 2H^+ \rightarrow 2V^{3+} + H_2O \quad (1.2)$$

$$V^{3+} + VO_2^+ \rightarrow 2VO^{2+} \quad (1.3)$$

$$V^{2+} + 2VO_2^+ + 2H^+ \rightarrow 3VO^{2+} + H_2O \quad (1.4)$$

Perfluorosulfonic acid (PFSA) membranes are widely used in VRFB due to good conductivity and excellent chemical and mechanical

* Corresponding author.
*E-mail address:* marco.cecchetti@polimi.it (M. Cecchetti).

https://doi.org/10.1016/j.est.2023.107846
Received 9 February 2023; Received in revised form 4 May 2023; Accepted 23 May 2023
Available online 1 June 2023

**Nomenclature**

| | |
|---|---|
| $Cap$ | Capacity $[C]$ |
| $C$ | Concentration $[mol\, m^{-3}]$ |
| $j$ | Current density $[A\, m^{-2}]$ |
| $D$ | Diffusivity $[m^{-2}\, s^{-1}]$ |
| $V_{sol}$ | Electrolyte solutions volume $[m^{-3}]$ |
| $F$ | Faraday's constant $[C\, mol^{-1}]$ |
| $d_f$ | Fibre diameter $[m]$ |
| $A_{geo}$ | Geometric area $[m^2]$ |
| $K$ | Kinetic constant $[m\, s^{-1}]$ |
| $h_{ch}$ | Mass transport coefficient in the distributor channel $[m\, s^{-1}]$ |
| $N$ | Molar flux $[mol\, m^{-2}\, s^{-1}]$ |
| $r_p$ | Pore radius $[m]$ |
| $V_p$ | Porous volume $[m^3 kg^{-1}]$ |
| $\phi$ | Potential [V] |
| $RR$ | Reaction Rate $[mol\, m^{-3} s^{-1}]$ |
| $a$ | Specific area $[m^{-1}]$ |
| $SoC$ | State of Charge $[-]$ |
| $SA$ | Surface Area $[m^2 kg^{-1}]$ |
| $T$ | Temperature $[K]$ |
| $l$ | Thickness $[m]$ |
| $\Delta t$ | Time step $[s]$ |
| $R$ | Universal gas constant $[J\, mol^{-1} K^{-1}]$ |
| $z$ | Valence $[-]$ |
| $\Delta V$ | Voltage $[V]$ |
| $i_v$ | Volumetric current density $[A\, m^{-3}]$ |
| $\dot{Q}$ | Volumetric flow rate $[m^3 s^{-1}]$ |

*Greek symbols*

| | |
|---|---|
| $\alpha$ | Charge transfer coefficient $[-]$ |
| $\eta$ | Overpotential $[V]$ |
| $\epsilon$ | Porosity $[-]$ |
| $\sigma$ | Conductivity $[S\, m^{-1}]$ |

*Superscripts*

| | |
|---|---|
| $b$ | Relative to the bulk electrolyte |
| $s$ | Relative to the electrode surface |
| $pos$ | Relative to the positive electrode |
| $neg$ | Relative to the negative electrode |
| $el$ | Relative to the electrode domain |
| $m$ | Relative to the membrane domain |
| $mem$ | Relative to the membrane domain |
| $eff$ | Effective |
| $L$ | Relative to the left boundary of the domain |
| $R$ | Relative to the right boundary of the domain |
| $ch$ | Relative to the distributor channel |
| $ch, el$ | Relative to the channel-electrode interface |
| $in$ | Relative to the inlet |
| $out$ | Relative to the outlet |

*Subscript*

| | |
|---|---|
| $i$ | Relative to the species $i$ |
| $l$ | Relative to the electrolytic phase |
| $s$ | Relative to the solid phase |
| $cx$ | Relative to cross-over |
| $pos$ | Relative to the positive electrode/electrolyte |
| $neg$ | Relative to the negative electrode/electrolyte |
| $M$ | Relative to the fixed charges in the membrane |
| $V^{2+}$ | Relative to the $V^{2+}$ species |
| $V^{3+}$ | Relative to the $V^{3+}$ species |
| $VO^{2+}$ | Relative to the $VO^{2+}$ species |
| $VO_2^+$ | Relative to the $VO_2^+$ species |
| $H^+$ | Relative to the $H^+$ species |
| $HSO_4^-$ | Relative to the $HSO_4^-$ species |
| $r$ | Relative to the iteration $r$ |

properties in the acidic environment of a VRFB. However, PFSA membranes are not ideally selective and vanadium ions can permeate through, thus battery manufacturer are forced to employ thick membranes (>50 μm) to mitigate cross-over fluxes, leading to high voltage losses through the membrane [13] and high capital costs (20 %–40 % of system capital costs) [14–16].

Given the high impact of the membrane on battery performance and cost, a large share of the VRFB related research focuses on the development of innovative separators as alternative to PFSA membranes [17,18]. A complete comprehension of cross-over phenomena and transport mechanisms is thus necessary to support the development of innovative separators and operating strategies for cross-over mitigation. In order to achieve that, the study of cross-over phenomena must be supported by a modelling analysis aimed at the evaluation of cross-over fluxes in a VRFB. The scientific literature presents several models describing the operation of a VRFB including vanadium transport through the membrane [10,12,19–36]. However, despite the involved phenomena and the governing equations are consolidated, different interpretations are present in the different studies because the definition of the model parameters deeply depends on the adopted validation process [37,38]. Oh et al. reported that diffusion and migration are the main mechanisms, while convection can be neglected since the velocity in the membrane is close to zero due to its low hydraulic permeability [19,30,31]. Gandomi et al. showed that diffusion is the predominant mechanism for cross-over fluxes at low current densities, but increasing the current density migration and diffusion contribute almost equally [25]. On the other hand, the works of Knehr et al. showed that convection and diffusions are the dominant mechanisms, while migration has a smaller influence [12,32,33]. Instead, Darling et al. showed that migration plays a significant role in the vanadium transport through the membrane at high current densities and thus it cannot be neglected [28]. Lei et al. also highlighted the influence of the Donnan effect, fixed charges concentration and selective ion adsorption on vanadium cross-over fluxes [10,35].

The different interpretations provided in literature are consequences of differences in the studies in the experimental hardware and operative conditions, which lead to uncertainties and differences on model parameters: for example the values of the vanadium ion diffusivities through the membrane can differ between the different studies even by one order of magnitude [25,37]. The uncertainties related to the model parameters are also due to the fact that in literature the calibration process of the models is usually conducted on a limited number of experimental data.

In particular, the models proposed in literature are validated and calibrated either on the overall capacity depletion of the battery during charge-discharge cycles with cut-off voltages [12,20,24,29,33] or only on the voltage of the first cycle neglecting battery self-discharge and capacity loss, often taking values for the diffusivities through the membrane from literature [10,19,21–23,26,27,30,31,34–36]. However, diffusivities values taken from literature commonly come from diffusion tests [21,25,39–41] which are straightforward tests to study the behaviour of a separator towards diffusion [42], but neglect migration which may be one the key transport mechanisms for vanadium cross-over: only Luo et al. [21] and Gandomi et al. [25] considered migration in their analysis of diffusion tests, although in ad-hoc designed experimental set-ups different from the real application.

As regards the calibration of diffusivities through the membrane on the capacity depletion of the battery during charge-discharge cycles with cut-off voltages, it introduces uncertainties on the resulting values as it does not take into account the self-discharge and imbalance of the single electrolytes. Moreover, the capacity loss during this type of cycles does not only depend on vanadium cross-over, but also on electrode degradation [43–45]. Therefore, the duration of each cycle is influenced both by vanadium cross-over and by electrode degradation: this introduces further uncertainties in the calibration of model parameters due to the complexity in isolating the two different phenomena. Furthermore, in the literature the calibration of different model parameters is usually conducted considering only one operating condition: just a limited works [22,27,30] validated their models on the voltage of a charge-discharge cycle at different operating current densities or on the results of a polarization curve. However, the capacity depletion of the battery or the electrolytes imbalance at different operating conditions were not considered. This induces in parameters that are not able to describe cross-over phenomena at different operating conditions, increasing the uncertainties related to the modelling analysis.

This work proposes a new approach for the calibration of models describing vanadium cross-over in VRFB, that is based on the utilization of charge-discharge cycles with fixed exchanged capacity and through-plate reference electrodes measurements. As described in Cecchetti et al. [45], imposing equal charged and discharged capacity at each cycle with constant current density allows to isolate the effects of cross-over from electrodes degradation on the evolution of the State of Charge (SoC) of the battery and of the two electrolytes, as the duration of each charge and discharge hemicycle is independent from the over-potential of the battery in this type of charge-discharge cycles. In this way, in absence of cross-over the SoC of the two electrolytes would be the same and constant after each charge and discharge. Otherwise, a decay of the Open Circuit Voltage (OCV) and of the Open Circuit Potentials (OCP) of the electrolytes, related to the SoC, can be observed in case of vanadium cross-over. The OCP of the two electrolytes is measured in-situ through the innovative system of through-plate reference electrodes firstly introduced in VRFB by the authors in Cecchetti et al. [45]. Moreover, this type of cycles facilitates the modelling analysis as the exchanged capacity is constant and it does not depend on the performance of the battery, therefore the impact of uncertainties of the model parameters related to the electrochemistry and mass transport inside the electrodes on the cross-over fluxes is limited.

In particular, a 1D physically-based model of the operation of a VRFB single cell is presented to support the analysis of cross-over fluxes of vanadium species through the ion exchange membrane of the battery. The Nernst-Planck equation is used to describe the flux of the species through the electrodes and the membrane to consider both migrative and diffusive fluxes. The model is calibrated on the results of charge-discharge cycles at three different current densities with fixed charged and discharged capacity presented in Section 4.1 by fitting kinetic and mass transport electrode parameters on the voltage of the battery, while the membrane parameters on the self-discharge and imbalance of the two vanadium electrolytes. This approach allows to obtain a more accurate calibration of the model with respect to fitting on the overall capacity depletion of the battery as it is done in literature. Furthermore, calibrating the model parameters on cycles at three different current densities allows to acquire model parameters that can effectively describe the migrative flux and the involved physics at different operating conditions.

It is worth mentioning that, although in this work a VRFB employing a Cation Exchange Membrane (CEM) is considered, the proposed approach can be easily applied to redox flow batteries with Anion Exchange Membranes (AEM). Indeed, the operation of the through-plate reference electrodes is not influenced by membrane typology and thus the self-discharge of the two electrolytes can be evaluated in both CEM and AEM systems. Moreover, also the physical-based model can be extended to describe the operation of batteries with AEM by modifying the governing equations to consider the different transported ionic charges.

## 2. Experimental

### 2.1. Experimental set-up

Fig. 1 reports a schematic representation of the experimental set-up employed in this work. The cell active area was 25 $cm^2$ with interdigitated distributor flow field at both positive and negative side of the cell. Both positive and negative electrodes were *Sigracet® 39AA* compressed to 230 μm (nominal thickness 290 μm) by exploiting glass-PTFE gaskets [46]. The membrane was *Nafion*™ N212 (50 μm thickness), used as received without any treatment.

The electrolyte solutions were prepared by dissolving vanadium (IV) sulfate oxide hydrate to obtain 1 M of vanadium ions in 5 M of sulphuric acid and by following to the procedure illustrated by Aaron al. [47].

Each test was performed with pristine electrodes, membrane and electrolyte solutions.

The electrolyte solutions were pressurized with nitrogen to avoid air intake and processed with a peristaltic pump (Watson-Marlow 323Du with a 314Dw 4 roller head pump).

Two through-plate hydrogen reference electrodes were applied at the cell, one for each side close to the inlet main channel inside the cell active area. As described in the authors previous works [45,48,49], this typology of reference electrodes consists in a *Nafion*™ tubing passing through the cell hardware acting as a salt bridge between the electrolyte in the electrode and a *Gaskatel HydroFlex®* reversible hydrogen electrode (RHE) immersed in 5 M sulphuric acid. This reference electrodes set-up allows to directly measure the OCP of the two electrodes to estimate the SoC of the two electrolyte solutions during the operation of the battery by exploiting the experimental SoC-OCP relationships derived in Cecchetti et al. [45].

Charge-discharge cycles and Electrochemical Impedance Spectroscopy (EIS) were performed with a high-precision high-speed source-measure unit (SMU) module *PXIe-4139* equipped on a *NI PXIe−1075* chassis by *National Instruments*.

### 2.2. Experimental tests

Charge and discharge cycles with fixed exchanged capacity with no cut-off voltages were performed at three different current densities: 10 mA $cm^{-2}$, 40 mA $cm^{-2}$ and 100 mA $cm^{-2}$. The exchanged capacity was 1875C for each charge and discharge, corresponding to a $\Delta SoC \sim 40$ % considering the total ideal capacity of the electrolyte solutions whose volume was 50 ml.[1] For each current density new electrolyte solutions were prepared and charged up until the OCV of the cell was 1.419 V, corresponding to a starting battery SoC of 40 %. After each charge and each discharge, the OCV and the OCP of the two half-cells were measured for 90 s to monitor the evolution of the battery self-discharge due to vanadium cross-over.[2]

An EIS was performed on the cell to measure the High Frequency Resistance (HFR) in OCV condition at 1.419 V with a sinusoidal current oscillation with 50 mA semi-amplitude at 50 frequencies ranging from 100 kHz to 1 Hz.

During all tests the volumetric flow rate of the electrolyte solutions was 40 ml $min^{-1}$.

[1] The value of the exchanged capacity was chosen to limit the SoC of the electrolytes after charge to prevent the evolution reaction of hydrogen at the negative side of the battery.

[2] The difference between the measure OCV of the battery and the OCV evaluated as the difference of the OCP of the positive electrode and OCP of the negative electrode was always lower than 5 mV during all tests.

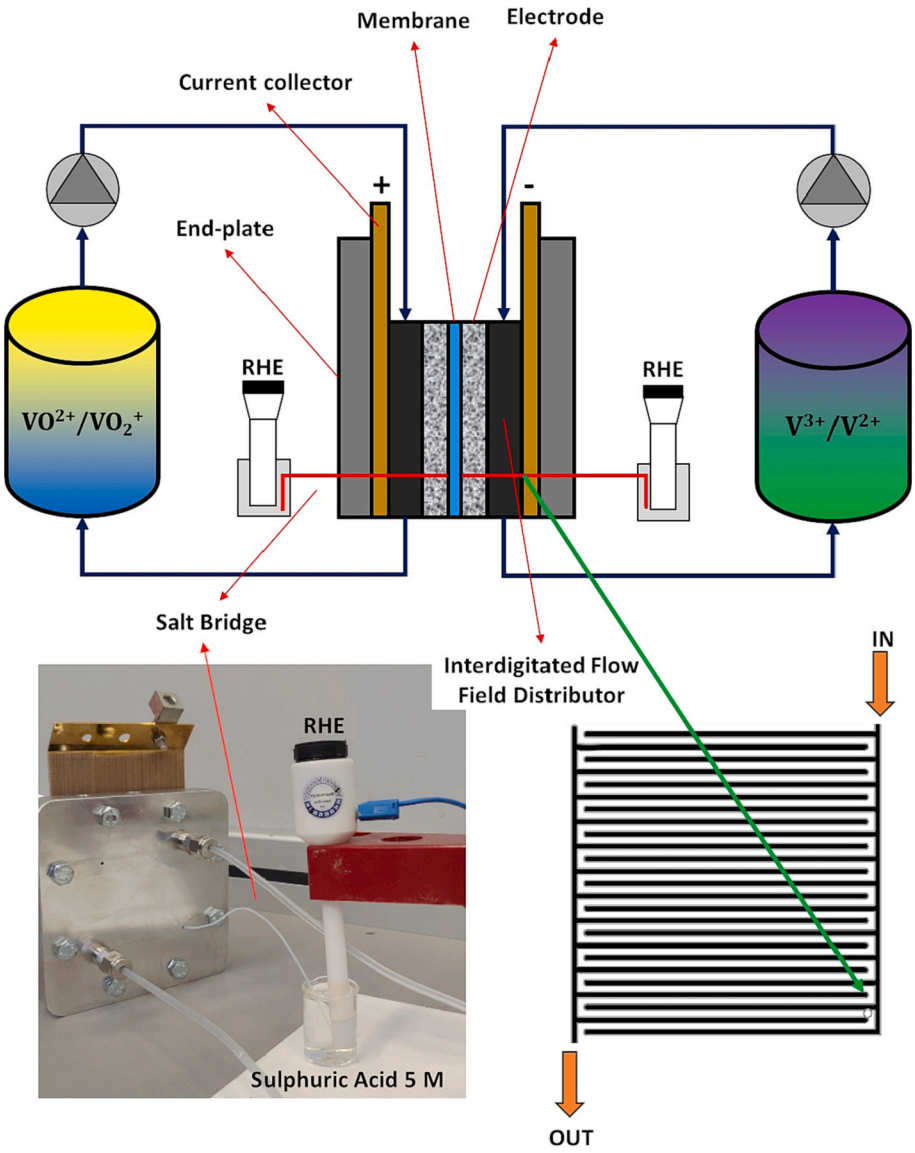


**Fig. 1.** Schematic representation of the experimental set-up (not to scale).

## 3. Model

### 3.1. Model assumptions and domains

The model describes the operation of a single cell VRFB during charge-discharge cycles at fixed exchanged capacity as series of stationary states. This hypothesis is justified by the fact that the cycling operations described with this model are at constant current with transients only at the beginning of each charge and each discharge which end within a time (~30 s) lower than the time step of the model iteration. The dimension of the model is 1D and it solves the variables in the direction along the coordinate x, which is the through-battery coordinate, as the model scheme in Fig. 2 shows. The domains described by the model are the positive and negative electrodes and the membrane. The modelled VRFB has a zero-gap architecture, meaning that the electrolyte is not directly injected through the electrode, but it is fed and withdrawn through a distributor. The mass transport inside the distributor channels is dealt with the boundary conditions. The 1D geometry was chosen to reduce the computational time, which is a critical resource in the modelling of long cycling operation. The assumption of 1D geometry is justified by the fact that the stoichiometry of the tests in Section 4.1 is in the range between 15.2 and 152,[3] leading thus to negligible concentration gradients along the direction of the channel. In literature several works adopted a reduced dimension in the modelling analysis of a VRFB [10,27,29,50–52]. In particular, Sharma et al. [53] identified the conditions for which it is possible to reduce the model dimension in the simulation of VRFB cell. In [53], the authors defined the nondimensional number $\Lambda$, which describes the relative change in the species concentration in the electrodes with respect to the total species concentration. In case of $\Lambda \ll 1$ it is possible to describe the VRFB cell with a dimension lower than 2D. In the operative conditions of the present work $\Lambda$ varies between $3.5 \times 10^{-3}$ and $3.5 \times 10^{-2}$, which is a range of values that satisfies the conditions set by Sharma et al. [53]. More details for the calculation of $\Lambda$ are provided in the Supplementary Materials. Also the work of Boettcher et al. [29] highlighted that reducing the dimension of the problem only introduces an error around

[3] Evaluated at 10 mA $cm^{-2}$, 40 mA $cm^{-2}$ and 100 mA $cm^{-2}$ considering 50 % SoC and 40 ml $min^{-1}$ volumetric flow rate.

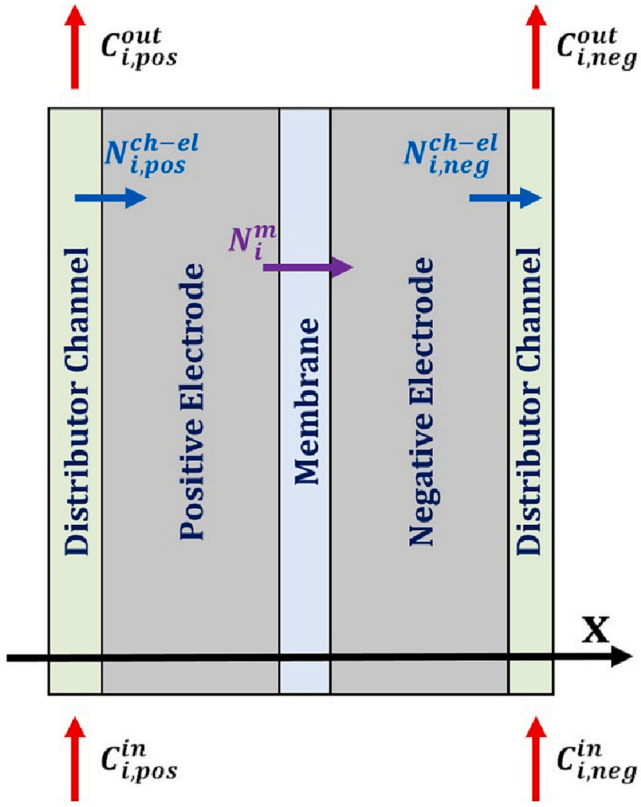


**Fig. 2.** Scheme of the domains described in the model (not to scale).

1 % on the capacity decay with respect to a 2D problem. Moreover, the ionic current in the membrane flows in the through-membrane direction, allowing to neglect gradients of the variables in the other directions [10].

The followings are the other hypothesis of the model:

- incompressible electrolyte solutions [10,12,34];
- isothermal system at a constant temperature of 298 K [10,12,51];
- uniformly mixed electrolytes in the external tanks [10,12,51];
- isotropic mass and charge transfer properties of electrodes, membrane and electrolyte [10,12];
- dilute solutions assumption for species transport [10,12];
- neglected hydrogen evolution reaction (HER) and oxygen evolution reaction (OER) [10,12][4];
- water transport through the membrane is neglected [10,22,26,34]

Moreover, the sulphuric acid employed in the electrolyte solutions is assumed to be fully dissociated in $H^+$ and $HSO_4^-$, while the second step of dissociation is neglected with a null concentration of $SO_4^{2-}$ all over the domains. This assumption is legitimized by the fact that the equilibrium constant for the second step of dissociation is very low and thus, given the high concentration of protons in the electrolytes employed in this work (5 M), the presence of $SO_4^{2-}$ is very unlikely.

As regards the assumption of neglected water transport, it derived from the fact that no significant volume change in the solutions was observed in the experimental tests reported in this work. This is consequence of the fact that the employed electrolytes had sulphuric acid concentration of 5 M, which allows to minimize the water transport through the separator [54–56].

The model describes the mass transport and electrochemistry in the positive and negative electrodes, as well as the species transport through the membrane.

The model, which is a multipoint boundary value problem, solves numerically the system of governing differential equations in the *MATLAB*™ environment through the *bvp5c* built-in function, whose algorithm is a finite difference code implementing the four-stage Lobatto IIIa formula [57]. The species described in the model are the four vanadium species, $V^{2+}$, $V^{3+}$, $VO^{2+}$ and $VO_2^+$, $H^+$ and $HSO_4^-$; while the variables solved by the models are:

- $C_i^b$, concentration of the species in the bulk electrolyte;
- $N_i$, molar flux of the species;
- $\phi_l$, liquid potential in the electrolytic phase;
- $\phi_s$, electric potential in the solid phase;
- $j_l$, ionic current density;
- $j_s$, electronic current density.

The model receives as input the inlet concentration of the involved species and the operating current density $j_{VRFB}$ of the VRFB and provides as output the distribution of the variables in the domains, the voltage of the battery, the potential of the electrodes, the potential losses through and the value of the cross-over fluxes. The input current density is taken positive during the charging of the battery.

In the following subsections the governing equations for each component are described.

### 3.1.1. Positive electrode

The molar balance of the species $V^{2+}$, $V^{3+}$, $VO^{2+}$, $VO_2^+$ and $H^+$ are defined by the following equations:

$$\nabla \bullet \overrightarrow{N_{V^{2+}}} = -2RR_{cx,1} - RR_{cx,2} - RR_{cx,4} \tag{3.1}$$

$$\nabla \bullet \overrightarrow{N_{V^{3+}}} = 3RR_{cx,1} + 2RR_{cx,2} - RR_{cx,3} \tag{3.2}$$

$$\nabla \bullet \overrightarrow{N_{VO^{2+}}} = -\frac{i_{v,pos}}{F} - RR_{cx,2} + 2RR_{cx,3} + 3RR_{cx,4} \tag{3.3}$$

$$\nabla \bullet \overrightarrow{N_{VO_2^+}} = \frac{i_{v,pos}}{F} - RR_{cx,1} - RR_{cx,3} - 2RR_{cx,4} \tag{3.4}$$

$$\nabla \bullet \overrightarrow{N_{H^+}} = 2\frac{i_{v,pos}}{F} - 4RR_{cx,1} - 2RR_{cx,2} - 2RR_{cx,4} \tag{3.5}$$

The terms on the right-hand side of these equations are the sources terms for the different species, considering both redox reactions of the $VO^{2+}/VO_2^+$ couple and the redox reactions described by Eqs. (1.1)–(1.4), whose reaction rates are indicated as $RR_{cx,k}$, which are modelled according to the following power laws:

$$RR_{cx,1} = K_{cx,1}\left(\frac{C^b_{V^{2+}}}{C_0}\right)^2\left(\frac{C^b_{VO_2^+}}{C_0}\right) \tag{3.6}$$

$$RR_{cx,2} = K_{cx,2}\left(\frac{C^b_{V^{2+}}}{C_0}\right)\left(\frac{C^b_{VO^{2+}}}{C_0}\right) \tag{3.7}$$

$$RR_{cx,3} = K_{cx,3}\left(\frac{C^b_{VO_2^+}}{C_0}\right)\left(\frac{C^b_{V^{3+}}}{C_0}\right) \tag{3.8}$$

$$RR_{cx,4} = K_{cx,4}\left(\frac{C^b_{VO_2^+}}{C_0}\right)^2\left(\frac{C^b_{V^{2+}}}{C_0}\right) \tag{3.9}$$

where $K_{cx,k}$ is the kinetic constant of the k-cross-over reaction and $C_0$ is the reference concentration equal to 1000 mol $m^{-3}$. As reported in Table 2, the values for the $K_{cx,k}$ were assumed to be $1 \times 10^6$ $mol\,m^{-3}s^{-1}$

[4] This assumption was further supported by the measurement of the potential of the electrodes in-operando with the RHE, which confirmed that the operation of the battery occurred in safe potential windows (Figure S1 of the Supplementary Materials).

to ensure that all cross-over reactions occur inside the electrode domains.

$i_{v,pos}$ in Eqs. (3.1)–(3.5) is the volumetric current density of the reaction of the redox couple $VO^{2+}/VO_2^+$ and is computed via Butler-Volmer equation:

$$i_{v,pos} = aFK_{pos}\left(C^s_{VO^{2+}} e^{\alpha_{pos}\frac{F}{RT}\eta_{pos}} - C^s_{VO_2^+} e^{\left(\alpha_{pos}-1\right)\frac{F}{RT}\eta_{pos}}\right) \tag{3.10}$$

with $a$ specific area, $K_{pos}$ kinetic constant of the reaction, $\eta_{pos} = \phi_s - \phi_l - E^{pos}_{0'}$ formal over-potential[5] of the reaction, $E^{pos}_{0'}$ formal equilibrium potential [51,58], $\alpha_{pos}$ charge transfer coefficient, $C^s_{VO^{2+}}$ and $C^s_{VO_2^+}$ concentrations at the electrode surface computed from the bulk ones as [50]:

$$C^s_{VO^{2+}} = C^b_{VO^{2+}} - \frac{i_{v,pos}}{\frac{aFD^{el}_{VO^{2+}}}{r_p}} \tag{3.11}$$

$$C^s_{VO_2^+} = C^b_{VO_2^+} + \frac{i_{v,pos}}{\frac{aFD^{el}_{VO_2^+}}{r_p}} \tag{3.12}$$

where $D^{el}_i$ is the diffusivity of the i-species in the electrolyte, while $r_p$ is the radius of the electrode pores.

The molar flux of each species is modelled with the Nernst-Planck equation:

$$\overrightarrow{N_i} = -D^{el,eff}_i \overrightarrow{\nabla C^b_i} - \frac{z_i F}{RT} D^{el,eff}_i C^b_i \overrightarrow{\nabla \phi_l} \tag{3.13}$$

from which the partial differential equation for the bulk concentrations of the vanadium species and protons can be obtained:

$$\overrightarrow{\nabla C^b_i} = -\frac{\overrightarrow{N_i}}{D^{el,eff}_i} - \frac{z_i C^b_i F}{RT}\overrightarrow{\nabla \phi_l} \tag{3.14}$$

where $z_i$ is the valence of the i-species, while $D^{el,eff}_i$ is the effective diffusivity in the electrode, which considers the porosity $\epsilon$ of the electrode according to the Bruggemann correlation [12]:

$$D^{el,eff}_i = D^{el}_i \epsilon^{1.5} \tag{3.15}$$

It is worth to mention that according to the Eq. (3.13) of the molar flux and to Eqs. (3.11) and (3.12) for the mass transport in the pores, convection inside the electrodes is neglected because of the impossibility of defining a velocity field for a 1D geometry. The influence of the volumetric flow rate of the electrolyte solutions is thus dealt with the boundary conditions.

Eq. (3.14) applies only for vanadium species and protons, while for the molar flux and bulk concentration of $HSO_4^-$ the electroneutrality is considered:

$$\sum_i z_i C^b_i = 0 \rightarrow C^b_{HSO_4^-} = -\frac{1}{z_{HSO_4^-}} \sum_{i \neq HSO_4^-} z_i C^b_i \tag{3.16}$$

$$\overrightarrow{j_l} = \sum_i z_i F \overrightarrow{N_i} \rightarrow \overrightarrow{N_{HSO_4^-}} = \frac{1}{z_{HSO_4^-}}\left(\frac{\overrightarrow{j_l}}{F} - \sum_{i \neq HSO_4^-} z_i \overrightarrow{N_i}\right) \tag{3.17}$$

Eq. (3.18) is the differential equation required by the *MATLAB*™ solver *bvp5c* for the electrolytic potential $\phi_l$, which is derived by multiplying Eq. (3.14) for each species by $z_i/D^{el,eff}_i$ and making the sum [50]:

$$\overrightarrow{\nabla \phi_l} = -\frac{RT}{F}\frac{\sum_i \frac{z_i \overrightarrow{N_i}}{D^{el,eff}_i}}{\sum_i z_i^2 C^b_i} \tag{3.18}$$

As regards the solid potential $\phi_s$, the Ohm's law is used to describe the relationship with the electronic current density $j_s$:

$$\overrightarrow{\nabla \phi_s} = -\frac{\overrightarrow{j_s}}{\sigma_s} \tag{3.19}$$

with $\sigma_s$ electric conductivity in the electrode. The last governing equations for the positive electrodes are the partial differential equations for $j_l$ and $j_s$:

$$\nabla \bullet \overrightarrow{j_l} = i_{v,pos} \tag{3.20}$$

$$\nabla \bullet \overrightarrow{j_s} = -i_{v,pos} \tag{3.21}$$

### 3.1.2. Negative electrode

The governing equations for the negative electrodes are the same of the positive electrode with some modification due to the different reaction involved. The molar balance of the species $V^{2+}$, $V^{3+}$, $VO^{2+}$, $VO_2^+$ and $H^+$ are defined in the negative electrode by the following equations:

$$\nabla \bullet \overrightarrow{N_{V^{2+}}} = -\frac{i_{v,neg}}{F} - 2RR_{cx,1} - RR_{cx,2} - RR_{cx,4} \tag{3.22}$$

$$\nabla \bullet \overrightarrow{N_{V^{3+}}} = \frac{i_{v,neg}}{F} + 3RR_{cx,1} + 2RR_{cx,2} - RR_{cx,3} \tag{3.23}$$

$$\nabla \bullet \overrightarrow{N_{VO^{2+}}} = -RR_{cx,2} + 2RR_{cx,3} + 3RR_{cx,4} \tag{3.24}$$

$$\nabla \bullet \overrightarrow{N_{VO_2^+}} = -RR_{cx,1} - RR_{cx,3} - 2RR_{cx,4} \tag{3.25}$$

$$\nabla \bullet \overrightarrow{N_{H^+}} = -4RR_{cx,1} - 2RR_{cx,2} - 2RR_{cx,4} \tag{3.26}$$

with $i_{v,neg}$ volumetric current density of the redox reactions of the $V^{2+}/V^{3+}$ couple, computed with Butler-Volmer equation:

$$i_{v,neg} = aFK_{neg}\left(C^s_{V^{2+}} e^{\alpha_{neg}\frac{F}{RT}\eta_{neg}} - C^s_{V^{3+}} e^{\left(\alpha_{neg}-1\right)\frac{F}{RT}\eta_{neg}}\right) \tag{3.27}$$

The concentration at the electrode surface can be calculated as:

$$C^s_{V^{2+}} = C^b_{V^{2+}} - \frac{i_{v,neg}}{\frac{aFD^{el}_{V^{2+}}}{r_p}} \tag{3.28}$$

$$C^s_{V^{3+}} = C^b_{V^{3+}} + \frac{i_{v,neg}}{\frac{aFD^{el}_{V^{3+}}}{r_p}} \tag{3.29}$$

The transport of the species is modelled via Nernst-Planck equation and therefore Eq. (3.14) applies also for the negative electrode and consequently also Eq. (3.18) for the gradient of the electrolytic potential. $HSO_4^-$ is dealt considering the electroneutrality, Eqs. (3.16) and (3.17), while the Ohm's law describes the gradient of $\phi_s$. The variation of the ionic and electronic current densities is determined by the volumetric current density of the redox reaction:

$$\nabla \bullet \overrightarrow{j_l} = i_{v,neg} \tag{3.30}$$

$$\nabla \bullet \overrightarrow{j_s} = -i_{v,neg} \tag{3.31}$$

### 3.1.3. Membrane

The membranes employed in this work are CEM and thus the amount of $HSO_4^-$ able to permeate into the membrane is limited due to the presence of negatively charged sulfonic groups. Therefore, the concentration and the flux of $HSO_4^-$ are assumed to be null. No reaction takes

[5] Overpotential calculated with respect to the formal equilibrium potential.

place inside the domain of the membrane and thus the source terms for the molar balance of the species are null:

$$\nabla \bullet \overrightarrow{N_i} = 0 \tag{3.32}$$

Moreover, since no reaction is occurring in the membrane the ionic current density is constant:

$$\nabla \bullet \overrightarrow{j_l} = 0 \tag{3.33}$$

The molar flux for each species is modelled with the Nernst-Planck equation and thus the partial differential equation for vanadium species and protons is:

$$\overrightarrow{\nabla C_i^b} = -\frac{N_i}{D_i^m} - \frac{z_i C_i^b F}{RT}\overrightarrow{\nabla \phi_l} \tag{3.34}$$

where $D_i^m$ is the diffusivity in *Nafion*™. Since the hydraulic permeability of the membrane is low, the convection through the membrane is neglected [31].

The gradient of the electrolytic potential in the membrane is calculated with the same equation of the electrodes:

$$\overrightarrow{\nabla \phi_l} = -\frac{RT}{F}\frac{\sum_i \frac{z_i \overrightarrow{N_i}}{D_i^m}}{\sum_i z_i^2 C_i^b} \tag{3.35}$$

Finally, in the membrane there is no solid phase and therefore $\phi_s$ and $j_s$ are not defined. However, *bvp5c* solves all variables in all domains, therefore $\phi_s$ and $j_s$ are set equal to 0 in the membrane through boundary conditions and the following partial differential equations for the solid phase variables:

$$\overrightarrow{\nabla \phi_s} = 0 \tag{3.36}$$

$$\nabla \bullet \overrightarrow{j_s} = 0 \tag{3.37}$$

### 3.1.4. Boundary conditions

The model defined by the governing equation listed previously is composed by 14 differential equations for 3 domains, therefore it requires 42 boundary conditions for the numerical resolution.

The continuity of the permeable species (vanadium species and protons) through the membrane must be guaranteed to respect the molar balance:

$$N_i^{pos,R} = N_i^{mem,L} \tag{3.38}$$

$$N_i^{mem,R} = N_i^{neg,L} \tag{3.39}$$

where *pos, mem and neg* refer to the positive electrode, membrane and negative electrode respectively, while R and L indicate the right or left boundary of the domain with respect the scheme of Fig. 2. Moreover, the ionic current density through the membrane must be equal to the operating current density of the battery $j_{VRFB}$ and it must be continuous at the interfaces of the domains:

$$j_l^{pos,R} = j_{VRFB} \tag{3.40}$$

$$j_l^{mem,L} = j_l^{pos,R} \tag{3.41}$$

$$j_l^{mem,R} = j_l^{neg,L} \tag{3.42}$$

As regards the electronic current density is set equal to the operating current density at the positive electrode left boundary and at the negative electrode right boundary, accordingly to the flow of electrons through the external circuit, while at the membrane interface is set to 0 for electric insultation:

$$j_s^{pos,L} = j_{VRFB} \tag{3.43}$$

$$j_s^{neg,R} = j_{VRFB} \tag{3.44}$$

$$j_s^{pos,R} = j_s^{mem,L} = 0 \tag{3.45}$$

$$j_s^{mem,R} = j_s^{neg,L} = 0 \tag{3.46}$$

At the interfaces between the electrodes and the distribution channels the boundary conditions must provide the information regarding the inlet concentrations and volumetric flow rate of the electrolyte solutions. Moreover, following the approach proposed by Zago and Casalegno [50] the flux at the channel-electrode interface is equal to a convective flux between the bulk concentration of the channel and at the interface:

$$N_i^{ch-el} = h_{ch,i}\left(C_i^{ch} - C_i^{ch,el}\right) \tag{3.47}$$

with $h_{ch,i}$ is the convective mass transport coefficient at the channel for i-species, while $C_i^{ch}$ is the bulk concentration in the channel that is evaluated as the average between the inlet and outlet concentration:

$$C_i^{ch} = \frac{C_i^{in} + C_i^{out}}{2} \tag{3.48}$$

However, $C_i^{out}$ is not known a priori since it depends on the flux of the species through the membrane and thus must be obtained by a molar balance on the distribution channel, which is modelled as a simple straight channel:

$$C_i^{out} = C_i^{in} - \frac{N_i^{el-ch} A_{geo}}{\dot{Q}} \tag{3.49}$$

where $A_{geo}$ is the geometrical area of the electrode and $\dot{Q}$ is the volumetric flow rate. After substituting Eqs. (3.49) and (3.48) in Eq. (3.47) and simple mathematical steps, the boundary condition for the electrode-channel interface is obtained:

$$N_i^{ch-el} = \frac{h_{ch,i}}{1 + \frac{h_{ch,i} A_{geo}}{2\dot{Q}}}\left(C_i^{in} - C_i^{ch-el}\right) \tag{3.50}$$

which can be rewritten in terms of the model variables for both positive and negative electrode-channel interfaces for the vanadium species and protons:

$$N_i^{pos,L} = \frac{h_{ch,i}}{1 + \frac{h_{ch,i} A_{geo}}{2\dot{Q}}}\left(C_i^{pos,in} - C_i^{pos,L}\right) \tag{3.51}$$

$$N_i^{neg,R} = \frac{h_{ch,i}}{1 + \frac{h_{ch,i} A_{geo}}{2\dot{Q}}}\left(C_i^{neg,R} - C_i^{neg,in}\right) \tag{3.52}$$

The convective mass transport coefficient can be obtained by the following correlation [50]:

$$h_{ch,i} = 7\frac{D_i^{el}}{d_f} Re^{0.4} \tag{3.53}$$

with $d_f$ average diameter of electrode fibres (8 μm [50]) and *Re* Reynolds number, equal to 0.044 computed assuming a velocity of 0.005 $m\ s^{-1}$ inside the porous electrode at 40 ml $min^{-1}$ according to the CFD analysis for an interdigitated flow field of Messaggi et al. [59].

At the interfaces between the electrodes and the membrane a discontinuity in the concentration of the species is presents due to the presence of the fixed charges in the membrane, thus in order to respect the electroneutrality the concentration of vanadium ions and protons have a step discontinuity at the interfaces. This phenomenon is known as Donnan effect and, due to the conservation of the electrochemical potential, it has consequently a discontinuity of the electrolytic potential, known as Donnan potential, as well:

$$\phi_l^{pos,R} - \phi_l^{mem,L} = \frac{RT}{z_{H^+}F} ln \frac{C_{H^+}^{mem,L}}{C_{H^+}^{pos,R}} \tag{3.54}$$

$$\phi_l^{mem,R} - \phi_l^{neg,L} = \frac{RT}{z_{H^+}F} ln \frac{C_{H^+}^{neg,L}}{C_{H^+}^{mem,R}} \tag{3.55}$$

Since the equations of the potential discontinuity are valid for each species, it is possible to express the discontinuity of the species as a function of the one of the $H^+$:

$$C_i^{mem,L} = C_i^{pos,R} \left( \frac{C_{H^+}^{mem,L}}{C_{H^+}^{pos,R}} \right)^{\frac{z_i}{z_{H^+}}} \tag{3.56}$$

$$C_i^{mem,R} = C_i^{neg,L} \left( \frac{C_{H^+}^{mem,R}}{C_{H^+}^{neg,L}} \right)^{\frac{z_i}{z_{H^+}}} \tag{3.57}$$

Electroneutrality inside the membrane is exploited to obtain the value of the proton concentration discontinuity, considering the fixed charges and the fact that $HSO_4^-$ is assumed null inside the membrane:

$$\sum_{i \neq HSO_4^-} z_i C_i^{pos,R} \left( \frac{C_{H^+}^{mem,L}}{C_{H^+}^{pos,R}} \right)^{\frac{z_i}{z_{H^+}}} + z_M C_M = 0 \tag{3.58}$$

$$\sum_{i \neq HSO_4^-} z_i C_i^{mem,R} \left( \frac{C_{H^+}^{neg,L}}{C_{H^+}^{mem,R}} \right)^{\frac{z_i}{z_{H^+}}} + z_M C_M = 0 \tag{3.59}$$

with $z_M$ and $C_M$ valence and concentration of the fixed charges in the membrane.

Finally, the solid phase potential at the negative electrode-channel interface is set to 0 as reference potential, while it is set as 0 at the membrane:

$$\phi_s^{neg,R} = \phi_s^{mem,R} = 0 \tag{3.60}$$

The voltage of the battery can be calculated as the difference between the solid phase potential of the positive and negative electrodes at the respective interfaces with the distributor channel:

$$\Delta V = \phi_s^{pos,L} - \phi_s^{neg,R} \tag{3.61}$$

### 3.2. Model of cycling operation

The proposed model is built in order to evaluate the cross-over fluxes during charge-discharge cycles with fixed exchanged capacity. The cycling operation of the battery is simulated with a succession of stationary states solved with the equations described in the previous subsection with input the charging or discharging current density and the inlet concentration at instant $r$ calculated from a molar balance at the electrolyte tank at the previous iteration $r$-1:

$$C_{i,r}^{pos,in} = C_{i,r-1}^{pos,in} - \frac{N_{i,r-1}^{pos,R} A_{geo}}{V_{sol}} \Delta t \tag{3.62}$$

$$C_{i,r}^{neg,in} = C_{i,r-1}^{neg,in} + \frac{N_{i,r-1}^{neg,L} A_{geo}}{V_{sol}} \Delta t \tag{3.63}$$

with $\Delta t$ time step of simulation and $V_{sol}$ volume of the electrolyte solution, assumed constant coherently with the experimental observations, as explained in Section 3.1.

Once the inlet concentrations are defined, it possible to calculate the SoC of the positive and negative electrolyte at each iteration:

$$SoC_r^{pos} = \frac{C_{VO_2^+,r}^{pos}}{C_{VO_2^+,r}^{pos} + C_{VO^{2+},r}^{pos}} \tag{3.64}$$

$$SoC_r^{neg} = \frac{C_{V^{2+},r}^{neg}}{C_{V^{2+},r}^{neg} + C_{V^{3+},r}^{neg}} \tag{3.65}$$

Moreover, it is possible to calculate the total capacity of the two electrolyte solutions at iteration $r$ from the total capacity at the previous iteration $r$-1 considering the moles of vanadium permeating through membrane:

$$Cap_{tot,r}^{pos} = Cap_{tot,r-1}^{pos} + \left( \left| N_{V^{2+}}^m \right| + \left| N_{V^{3+}}^m \right| - \left| N_{VO^{2+}}^m \right| - \left| N_{VO_2^+}^m \right| \right) FA_{geo} \Delta t \tag{3.66}$$

$$Cap_{tot,r}^{neg} = Cap_{tot,r-1}^{neg} + \left( \left| N_{VO^{2+}}^m \right| + \left| N_{VO_2^+}^m \right| - \left| N_{V^{2+}}^m \right| - \left| N_{V^{3+}}^m \right| \right) FA_{geo} \Delta t \tag{3.67}$$

where $N_i^m$ is the molar flux through the membrane, which is constant through the membrane. As it can be seen from Eqs. (3.66) and (3.67), the total capacity of one side decreases as the module of the flux of its species increases and increases as the flux of the species from the other side increases. The capacity of the two electrolyte solutions can be calculated as:

$$Cap_r^{pos} = Cap_{tot,r}^{pos} SoC_r^{pos} \tag{3.68}$$

$$Cap_r^{neg} = Cap_{tot,r}^{neg} SoC_r^{neg} \tag{3.69}$$

$Cap_r^{pos}$ and $Cap_r^{neg}$ accounts for the capacity stored in the charged species of both electrolytes at instant $r$ and thus it can be also written with respect the value of the previous iteration $r$-1 by adding the capacity charged or discharged during the operation and the self-discharge due to cross-over:

$$Cap_r^{pos} = Cap_{r-1}^{pos} + \left( \frac{j_{VRFB}}{F} - \left| N_{VO_2^+}^m \right| - 2 \left| N_{V^{2+}}^m \right| - \left| N_{V^{3+}}^m \right| \right) FA_{geo} \Delta t \tag{3.70}$$

$$Cap_r^{neg} = Cap_{r-1}^{neg} + \left( \frac{j_{VRFB}}{F} - \left| N_{V^{2+}}^m \right| - 2 \left| N_{VO_2^+}^m \right| - \left| N_{VO^{2+}}^m \right| \right) FA_{geo} \Delta t \tag{3.71}$$

The term $\frac{j_{VRFB}}{F}$ takes into account the faradaic charge and discharge of the battery, the second term in the parentheses is the loss of capacity due to charged species permeating to the other side of cell, while the third and fourth represents the self-discharge due to cross-over of vanadium species from the other side. Combining equations from Eqs. (3.66) to (3.71), it is possible to obtain an alternative expression for the SoCs:

$$SoC_r^{pos} = \frac{Cap_r^{pos}}{Cap_{tot,r}^{pos}} = \frac{Cap_{r-1}^{pos} + \left( \frac{i_{VRFB}}{F} - \left| N_{VO_2^+}^m \right| - 2 \left| N_{V^{2+}}^m \right| - \left| N_{V^{3+}}^m \right| \right) FA_{geo} \Delta t}{Cap_{tot,r-1}^{pos} + \left( \left| N_{V^{2+}}^m \right| + \left| N_{V^{3+}}^m \right| - \left| N_{VO^{2+}}^m \right| - \left| N_{VO_2^+}^m \right| \right) FA_{geo} \Delta t} \tag{3.72}$$

$$SoC_r^{neg} = \frac{Cap_r^{neg}}{Cap_{tot,r}^{neg}} = \frac{Cap_{r-1}^{neg} + \left( \frac{i_{VRFB}}{F} - \left| N_{V^{2+}}^m \right| - 2 \left| N_{VO_2^+}^m \right| - \left| N_{VO^{2+}}^m \right| \right) FA_{geo} \Delta t}{Cap_{tot,r-1}^{neg} + \left( \left| N_{VO^{2+}}^m \right| + \left| N_{VO_2^+}^m \right| - \left| N_{V^{2+}}^m \right| - \left| N_{V^{3+}}^m \right| \right) FA_{geo} \Delta t} \tag{3.73}$$

Eqs. (3.72) and (3.73) show the complexity of the effect of cross-over phenomena on the SoC of the battery and of the electrolyte solutions. For example, since the flux of $VO_2^+$, the charged species of the positive electrolyte, is at both numerator and denominator of Eq. (3.72), its permeation through the membrane causes at the same time a reduction of the charged species at the positive electrolyte and a reduction of the total capacity, which have opposed effects on the SoC of the positive electrolyte. Moreover, the fluxes of $V^{2+}$ and $V^{3+}$ have a detrimental influence on the SoC by both reducing the numerator through cross-over reactions and increasing the denominator by increasing the amount of vanadium in the electrolyte.

This complexity proves that it is not possible to have an accurate analysis of the cross-over phenomena by just looking at the experimental data, but it requires a proper modelling analysis. For the model to be

able to accurately reproduce the physics of vanadium cross-over, a proper calibration on the experimental data must be achieved.

## 4. Results and discussion

### 4.1. Charge-discharge cycles with fixed exchanged capacity

Fig. 3 reports the OCV of the battery and the OCP of the two electrolyte solutions after each charge and discharge and their corresponding SoC, evaluated exploiting the experimental relationship derived in Cecchetti et al. [45]. As Fig. 3A shows, comparing at the same number of cycles, the lowest self-discharge of the battery occurred in the case of current density 100 mA $cm^{-2}$, while at 10 mA $cm^{-2}$ the highest self-discharge was observed. The large self-discharge in the case of 10 mA $cm^{-2}$ led to a first OCV after charge significantly lower (~11 mV) than the other cases, corresponding to a loss of SoC of nearly 3.5 %. Therefore, at 100 mA $cm^{-2}$ the battery was able to perform more cycles and thus it allowed to exchange a larger overall capacity. However, the time of a single cycle was not the same in the three cases due to the different applied current: for example, a cycle for the 10 mA $cm^{-2}$ case lasted 10 times longer than the 100 mA $cm^{-2}$. Therefore, it is also worth comparing the self-discharge after the same cycling time: at the end of each test the SoC of battery was similar in the three cases, with differences in the range of 1 % SoC. Therefore, the experimental results may suggest that the self-discharge rate due to cross-over does not depend significantly on the applied current density comparing the test at the same time. However, solid conclusions can be drawn only with a modelling analysis due the complex interplay of involved phenomena, as it will be proposed in Section 4.3.

As regards the self-discharge of the single electrolyte solutions, shown in Fig. 3B and C, comparing at the same number of cycles, the SoC of the two electrolytes decreased more slowly when the current density increased. However, similarly to the evolution of the OCV, at the end of the test the difference in the SoCs were lower than 5 % for both positive and negative electrolyte. At each current density the positive electrolyte suffered a faster self-discharge than the negative electrolyte as at the end of the charge of last cycle the SoC of the negative electrolyte was between 70 % and 74 %, while for the positive electrolyte it was between 60 % and 65 %. Moreover, the variation between the beginning and the end of test in the SoC of the two electrolytes (Fig. 3B and C) presented no significant differences among the three current densities. This confirms the absence of side reactions, which would have led to a significantly larger self-discharge in the case of 100 mA $cm^{-2}$. Fig. S1 of the Supplementary Materials reports the potentials of the positive and negative electrodes measured with the RHE, which showed that the operation occurred in safe potential windows.

To provide a solid interpretation of these experimental data, a modelling analysis is proposed in the following section.

### 4.2. Model calibration

The voltage of the first cycle and the self-discharge of the positive and negative electrolytes during the charge-discharge cycles at three different current densities were used to calibrate the model presented in Section 3. Calibrating the data at different current densities allows to obtain parameters able to describe electrochemistry and the mass transport in different operating conditions. In particular, the fitted parameters were $K_{pos}$ and $K_{neg}$, kinetic constants of the positive and negative electrode reactions, $D_i^{el}$, diffusivities of the involved species in the electrolyte, and $D_i^m$, diffusivities in the membrane. The remaining parameters were either assumed or taken from literature, as indicated in Tables 1 and 2. In order to improve the accuracy of the calibrated parameters, each parameter was fitted on the data more sensitive to the considered parameter accordingly to a preliminary sensitivity analysis. In particular, $K_{pos}$, $K_{neg}$ and $D_i^{el}$, being responsible of the performance of the battery, were calibrated with the voltages of the first cycle of the three different current densities, when the effect of cross-over phenomena on performance is more limited. $D_{H^+}^m$ was calibrated in order to have a potential loss through the separator coherent with the value of the HFR from the EIS (250.7 mΩ $cm^2$, Figs. S2 and S3 of the Supplementary Materials). $D_i^m$ of $V^{2+}$and $V^{3+}$ on the self-discharge of the positive electrolyte, while $D_i^m$ of $VO^{2+}$and $VO_2^+$ on the self-discharge of the negative electrolyte. Fitting the membrane diffusivities on the self-discharge of each electrolyte solutions allows to consider the effect of each vanadium species on the self-discharge and thus to obtain a more accurate calibration of these parameters with respect to fitting on the overall capacity decay of the battery, as usually done in literature [12,20,24,29,33]. The model calibration was conducted iteratively to consider the interaction between the different model parameters. In particular, $D_{H^+}^m$ was firstly calibrated on the potential loss through the membrane accordingly to the value of the HFR. Then $K_{pos}$, $K_{neg}$ and $D_i^{el}$ were tuned on the voltages of the first cycle at the three different current densities by reducing the root mean square error (RMSE) between model simulations and experimental data. After that, $D_{V^{2+}}^m$, $D_{V^{3+}}^m$, $D_{VO^{2+}}^m$ *and* $D_{VO_2^+}^m$ were adjusted to minimize the RMSE on the self-discharge of the two electrolytes at the three different current densities. Since all the calibrated parameters simultaneously influence with a different intensity the potential loss through the membrane, the voltages of the first cycle and the self-discharge of the two electrolytes, the described calibration procedure was repeated iteratively. The first calibration steps were performed manually by changing one parameter at a time in order to carefully monitor the evolution of the different physical quantities and then a Particle Swarm Optimization (PSO) algorithm [60] was adopted for a finer tuning of the parameters. The iterative calibration process is time consuming, but it allows to reduce the uncertainties of the model parameters, improving the accuracy of the model predictions.

Fig. 4 reports the comparison between the experimental data of the voltage of the first cycles at the three different current densities and the calculated with the model. As it can be seen from the figure, the model is able to reproduce with good accuracy the voltage of the first cycle at all current densities with a RMSE equal to 3.87 mV at 10 mA $cm^{-2}$, 5.43 mV at 40 mA $cm^{-2}$ and 5.42 mV at 100 mA $cm^{-2}$.

Table 1 reports the value of model parameters. The kinetic constants of the positive and negative reactions $K_{pos}$ and $K_{neg}$ are very variable in the literature due to the different electrodes employed by the different works, which present different activities, and also different cell architecture [61]. However, the resulting values are coherent with the ones reported in previous works. For example, $K_{neg}$ is in the same order of magnitude of the one proposed by Knehr et al. ($7 \times 10^{-8}\ m\ s^{-1}$) [12]. As regards $K_{pos}$, it is higher than $K_{neg}$ coherently with the results of Cecchetti et al. [49], in which it was proved that the negative reaction is more kinetically limited by the positive one in the case of 39AA carbon paper electrodes. Lei et al., He et al. and You et al. [10,62,63] also reported a kinetic constant higher for the positive reaction. Another factor that contributes to the variability of the value of the kinetic constant is the specific area: the carbon felts used in [10,12,22,62,63] have large pores, resulting in a relatively low specific area with values in the range $1 \times 10^4 - 3.5 \times 10^4\ m^{-1}$, while 39AA has smaller pores, but the carbon flakes on the fibres offers an higher surface area with a resulting specific area of $3.75 \times 10^5\ m^{-1}$, one order of magnitude higher than the carbon felt. The value of the specific area has been calculated from the value of the specific porous volume $V_p$ and surface area $SA$ measured via Mercury Intrusion Porosimetry in Cecchetti et al. [49]:

$$a = \frac{SA}{V_p} \tag{4.1}$$

The electrolyte diffusivities in the electrode fitted in this work are higher than the ones presented in literature [10,12,22,62,63]:

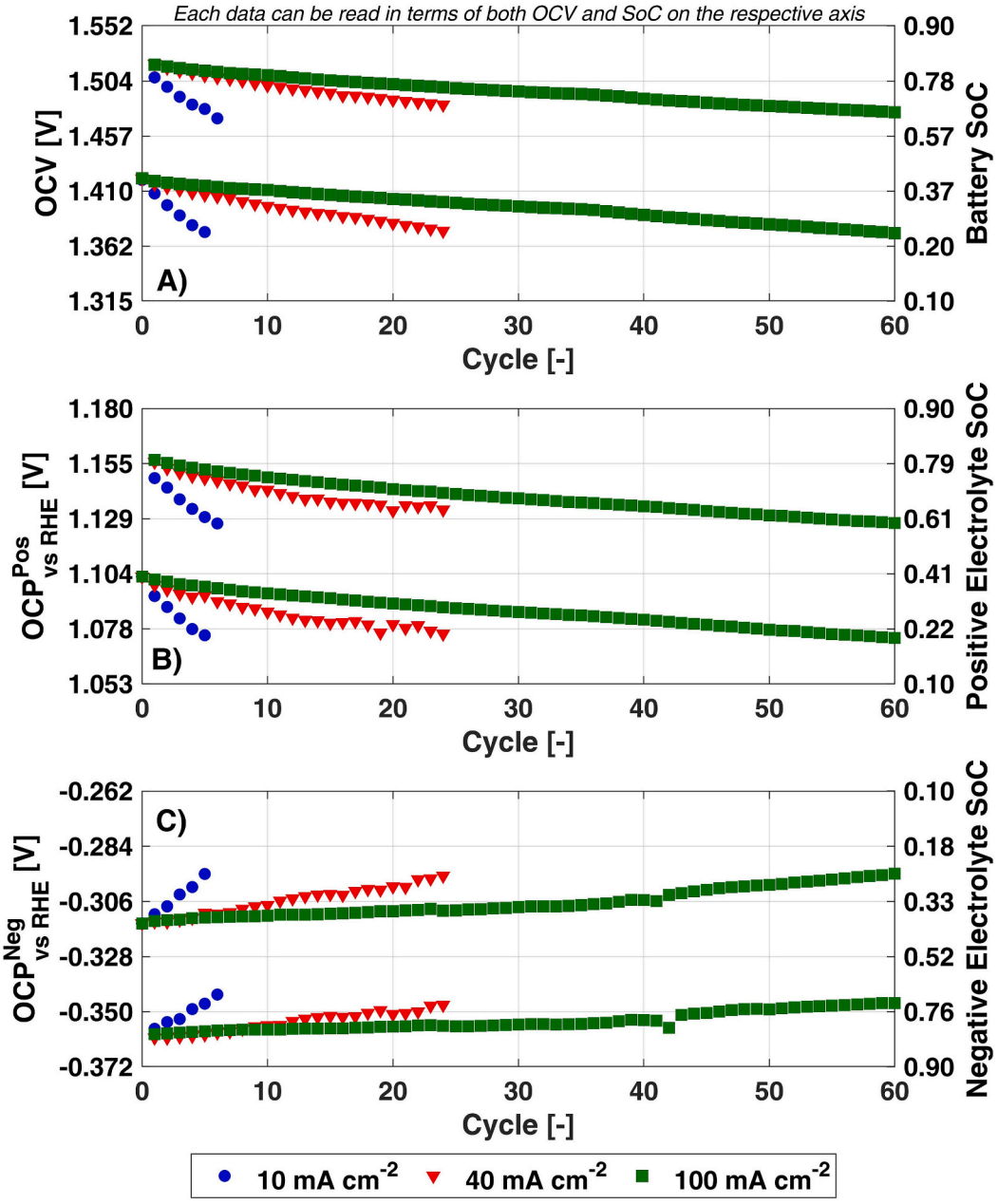


**Fig. 3.** A)Battery OCV (left axis) and corresponding SoC (right axis) evolution during charge-discharge cycles with fixed exchanged capacity at different current densities. B) Positive electrolyte and C) negative electrolyte OCP measured by RHE and corresponding SoC during charge-discharge cycles with fixed exchange capacity.

considering that the proposed model is 1D and it does not solve the complex fluid-dynamics in the channels and in the porous electrodes, higher values of diffusivities can be considered acceptable [50].

Fig. 5 shows the self-discharge for both electrolytes at the three different current densities, comparing the experimental data and the calculated SoC. As it can be seen, the model is able to reproduce the trend of the self-discharge of both electrolytes at all current densities with a maximum RMSE on the SoC of 2.6 % after charge at 40 mA $cm^{-2}$ for the positive electrolyte, and a RMSE of 4.9 % after discharge at 10 mA $cm^{-2}$ for the positive electrolyte as reported in Table S2 of the Supplementary Materials.

The parameters relative to the species transport in the membrane and the cross-over reactions are reported in Table 2. The fitted proton diffusivity through *Nafion*™ is coherent with literature, where values between $3.35 \times 10^{-9}\ m^2\ s^{-1}$ and $3.5 \times 10^{-10}\ m^2\ s^{-1}$ are proposed [10,12,22]. The diffusivities through the membrane of the negative electrolyte are higher than the ones of the positive electrolyte. This is coherent with the results of the charge-discharge cycles reported in Fig. 3, where the self-discharge of the positive electrolyte was higher compared to negative electrolyte. Table 3 compares the value of the diffusivities in the membrane for the vanadium species with the values found in literature [12,21,25,41]. As it can be seen, there is variability in the proposed diffusivities and discrepancy on which is the species with the highest diffusivities. However, the resulting values are in the range of the value presented in literature, with the exception of the diffusivity of $V^{2+}$ which is slightly higher than the value proposed by Luo et al. [21], but in the same order of magnitude.

A sensitivity analysis on the calibrated parameters was conducted to assess the confidence of the fitted parameters. The sensitivity analysis showed that most of the calibrated parameters have a confidence bound

**Table 1**
Assumed, fitted or taken from literature model parameters regarding the electrochemistry and mass transport inside the electrodes.

| Parameter | | Value | Ref. |
|---|---|---|---|
| Temperature | $T$ | $298\ K$ | – |
| Cell area | $A_{geo}$ | $25 \times 10^{-4}\ m^2$ | – |
| 39AA compressed porous volume | $V_p$ | $3.2 \times 10^{-6}\ m^3 g^{-1}$ | [49] |
| 39AA surface area | SA | $1.2\ m^2 g^{-1}$ | [49] |
| Specific area | a | $3.75 \times 10^5\ m^{-1}$ | $SA/V_p$ |
| Electrode thickness | $l_{el}$ | $220 \times 10^{-6}\ m$ | [49] |
| Pores radius | $r_p$ | $50 \times 10^{-6}\ m$ | [49] |
| Electrode porosity | $\epsilon$ | 0.9 | [50] |
| Electrode electric conductivity | $\sigma_S$ | $1000\ S\ m^{-1}$ | [50] |
| Formal equilibrium potential $V^{2+}/V^{3+}$ | $E^{neg}_{0'}$ | $-0.332\ V$ | Fitted on the data of [45] |
| Formal equilibrium potential $VO^{2+}/VO_2^+$ | $E^{pos}_{0'}$ | $1.121\ V$ | Fitted on the data of [45] |
| Negative charge transfer coefficient | $\alpha_{neg}$ | 0.5 | Assumed |
| Positive charge transfer coefficient | $\alpha_{pos}$ | 0.5 | Assumed |
| Negative kinetic constant | $K_{neg}$ | $6.69 \times 10^{-8}\ m\ s^{-1}$ | Fitted on cell voltage |
| Positive kinetic constant | $K_{pos}$ | $1.76 \times 10^{-6}\ m\ s^{-1}$ | Fitted on cell voltage |
| Electrolyte diffusivity $V^{2+}$ | $D^{el}_{V^{2+}}$ | $2.02 \times 10^{-9}\ m^2\ s^{-1}$ | Fitted on cell voltage |
| Electrolyte diffusivity $V^{3+}$ | $D^{el}_{V^{3+}}$ | $2.73 \times 10^{-9}\ m^2\ s^{-1}$ | Fitted on cell voltage |
| Electrolyte diffusivity $VO^{2+}$ | $D^{el}_{VO^{2+}}$ | $2.32 \times 10^{-9}\ m^2\ s^{-1}$ | Fitted on cell voltage |
| Electrolyte diffusivity $VO_2^+$ | $D^{el}_{VO_2^+}$ | $1.66 \times 10^{-9}\ m^2\ s^{-1}$ | Fitted on cell voltage |
| Electrolyte diffusivity $H^+$ | $D^{el}_{H^+}$ | $9.25 \times 10^{-9}\ m^2\ s^{-1}$ | Fitted on cell voltage |
| Electrolyte diffusivity $HSO_4^-$ | $D^{el}_{HSO_4^-}$ | $1.38 \times 10^{-9}\ m^2\ s^{-1}$ | Fitted on cell voltage |

**Table 2**
Assumed, fitted or taken from literature model parameters regarding the species transport through the membrane and the cross-over reactions.

| Parameter | | Value | Ref. |
|---|---|---|---|
| Cross-over reaction rate constant | $K_{cx,k}$ | $1 \times 10^6\ mol\ m^{-3} s^{-1}$ | assumed |
| Membrane thickness | $l_m$ | $50 \times 10^{-6}\ m$ | – |
| Membrane diffusivity $V^{2+}$ | $D^m_{V^{2+}}$ | $1.30 \times 10^{-11}\ m^2\ s^{-1}$ | fitted on positive electrolyte self-discharge |
| Membrane diffusivity $V^{3+}$ | $D^m_{V^{3+}}$ | $1.25 \times 10^{-11}\ m^2\ s^{-1}$ | fitted on positive electrolyte self-discharge |
| Membrane diffusivity $VO^{2+}$ | $D^m_{VO^{2+}}$ | $3.81 \times 10^{-12}\ m^2\ s^{-1}$ | fitted on negative electrolyte self-discharge |
| Membrane diffusivity $VO_2^+$ | $D^m_{VO_2^+}$ | $3.10 \times 10^{-12}\ m^2\ s^{-1}$ | fitted on negative electrolyte self-discharge |
| Membrane diffusivity $H^+$ | $D^m_{H^+}$ | $5.83 \times 10^{-10}\ m^2\ s^{-1}$ | fitted on membrane potential loss |
| Membrane fixed charges concentration | $C_M$ | $1280\ mol\ m^{-3}$ | [22] |
| Membrane fixed charges valence | $z_M$ | -1 | [22] |

of ±5% or ±10%. The results of the sensitivity analysis are reported the Supplementary Materials (Figs. S4 and S5).

After model calibration it is possible to exploit the developed model to investigate the influence of the operating current density on the vanadium cross-over phenomena. In particular, it was studied how the flux of the vanadium species through the membrane changes according to the current.

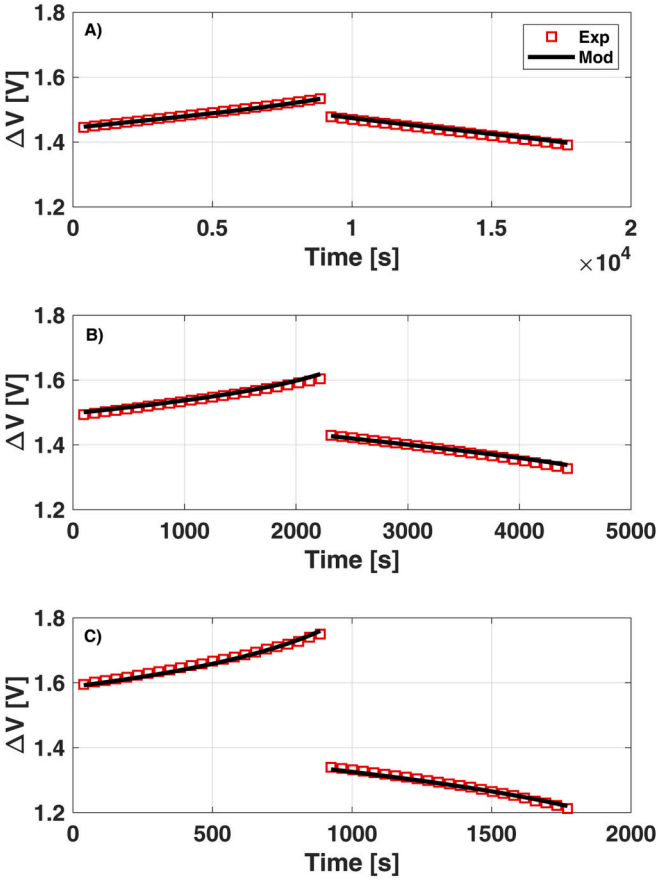


**Fig. 4.** Experimental and calculated first cycle voltage A) 10 mA $cm^{-2}$ B) 40 mA $cm^{-2}$C) 100 mA $cm^{-2}$.

### 4.3. Cross-over fluxes analysis

Fig. 6A,C,E reports the values of the average molar fluxes, calculated as integral averages, during charge, discharge and on the whole duration of the test, respectively.[6] During charge, Fig. 6A, the average flux of the species of the positive electrolyte $VO^{2+}$ and $VO_2^+$ increases with the current density, while for the negative electrolyte species, $V^{2+}$ and $V^{3+}$, it decreases. In discharge, Fig. 6C, the behaviour is the opposite with an increasing flux for the negative electrolyte species and decreasing for the positive ones. This behaviour is coherent with the direction of the electrolytic potential gradient, whose absolute value increases with the current density. Indeed, during charge the electrolytic potential in the membrane decreases towards the negative electrode along the x-axis accordingly to Fig. 2. This favours the flux of species of the positive electrolyte and inhibits the flux of negative electrolyte species accordingly to the Nernst-Planck Eq. (3.13). Instead, in discharge the gradient has the opposite direction and thus the flux of $VO^{2+}$ and $VO_2^+$ is inhibited, while the flux of $V^{2+}$ and $V^{3+}$ is enhanced. As regards the average on the whole test, Fig. 6E, the flux of each species increases with the current and it is always higher for the negative species at the investigated operating current density. This implies a net vanadium transport from the negative electrolyte the positive electrolyte, which decreases by 19 % with increasing current from $6.35 \times 10^{-6}\ mol\ m^{-2}\ s^{-1}$

[6] The average fluxes are all reported as positive to facilitate the comparison and the analysis, thus in Figure 6 a positive value does not refer to the direction of the flux. The average fluxes of the positive electrolyte species are always directed towards the negative electrolyte, while the ones of the negative electrolyte species towards the positive electrolyte.

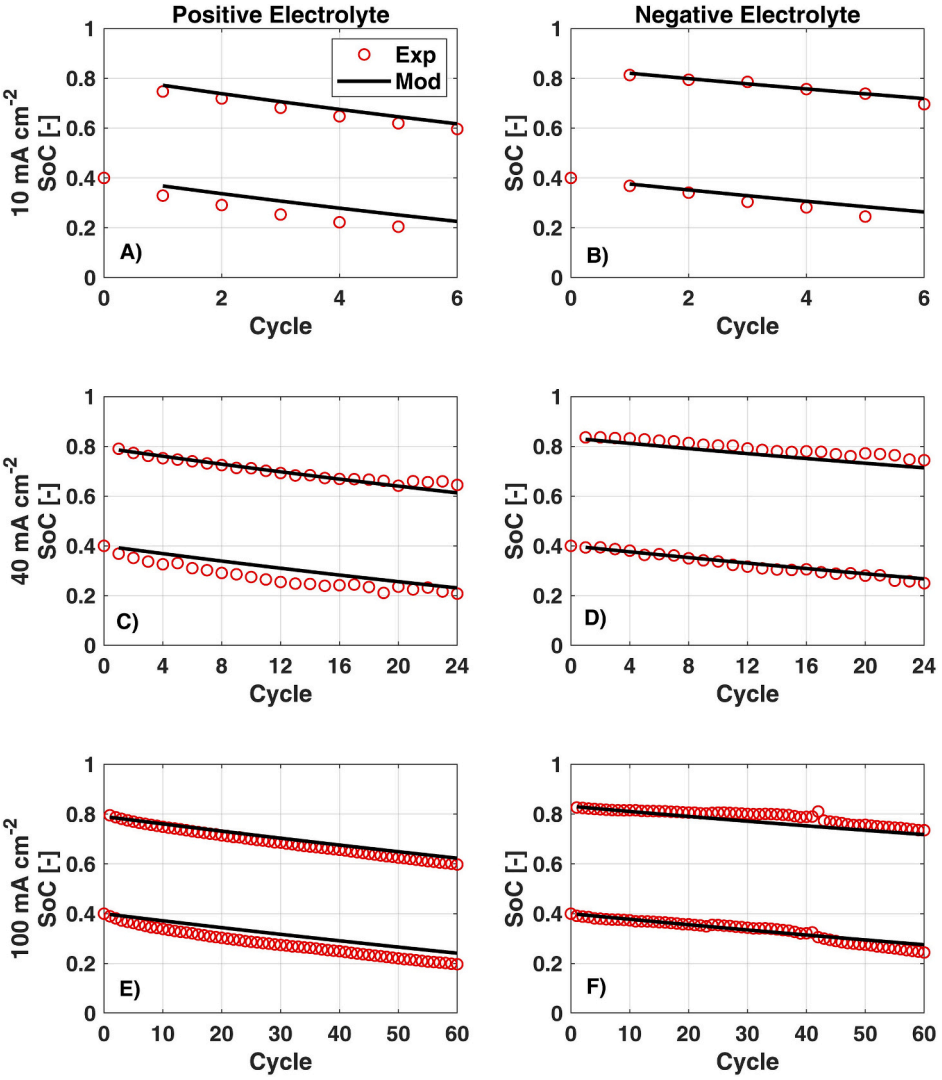


**Fig. 5.** Experimental vs calculated SoC at three different current densities: A, C, E) Positive electrolyte B, D, F) Negative electrolyte. A, B) 10 mA $cm^{-2}$, C, D) 40 mA $cm^{-2}$ E, F) 100 mA $cm^{-2}$.

**Table 3**
Comparison of the calibrated diffusivities in the membrane with the values reported in literature.

| Ref. | $D^m_{V^{2+}}\ [m^2 s^{-1}]$ | $D^m_{V^{3+}}\ [m^2 s^{-1}]$ | $D^m_{VO^{2+}}\ [m^2 s^{-1}]$ | $D^m_{VO_2^+}\ [m^2 s^{-1}]$ |
|---|---|---|---|---|
| This work | $13.00 \times 10^{-12}$ | $12.50 \times 10^{-12}$ | $3.81 \times 10^{-12}$ | $3.10 \times 10^{-12}$ |
| Knehr et al. [12] | $3.13 \times 10^{-12}$ | $5.93 \times 10^{-12}$ | $5.00 \times 10^{-12}$ | $1.17 \times 10^{-12}$ |
| Luo et al. [21] | $9.44 \times 10^{-12}$ | $14.50 \times 10^{-12}$ | $4.45 \times 10^{-12}$ | $2.40 \times 10^{-12}$ |
| Gandomi et al. [25] | $3.39 \times 10^{-12}$ | $1.87 \times 10^{-12}$ | $2.84 \times 10^{-12}$ | $2.32 \times 10^{-12}$ |
| Sun et al. [41] | $8.77 \times 10^{-12}$ | $3.22 \times 10^{-12}$ | $6.83 \times 10^{-12}$ | $5.90 \times 10^{-12}$ |

at 10 mA $cm^{-2}$ to $5.12 \times 10^{-6}$ $mol\, m^{-2}\, s^{-1}$ at 100 mA $cm^{-2}$. Therefore, operating at higher current density helps in reducing the net vanadium transport from the negative to the positive electrolyte.

According to the cross-over reactions reported in Eqs. (1.1)–(1.4), the effect on electrolytes self-discharge is different for each species, therefore the analysis must be extended also to the cross-over reactions rate. Fig. 6B,D,F reports the average cross-over reactions rate for the two electrolytes at the different operating conditions quantified as the parasitic current density associated to the cross-over reactions, calculated from the average fluxes as:

$$j^{pos}_{CX} = (2\overline{N_{V^{2+}}} + \overline{N_{V^{3+}}})F \tag{4.2}$$

$$j^{neg}_{CX} = \left(2\overline{N_{VO_2^+}} + \overline{N_{VO^{2+}}}\right)F \tag{4.3}$$

Considering the trend of the cross-over reactions rate with the operating current density during charge (Fig. 6B), it can be observed that it increases for the negative electrolyte accordingly to Eq. (4.3) as the cross-over fluxes from the positive electrolyte increases with the current density, as shown in Fig. 6A. Similarly, it decreases for the positive electrolyte due to the reduction of the fluxes from the negative half-cell accordingly to Fig. 6A. As regards the discharge (Fig. 6D), the cross-over reactions rate for the positive electrolyte increases with the operating current density due to the larger fluxes from the negative electrolyte (Fig. 6C), while it decreases for the negative electrolyte. Therefore, the trends of the cross-over reactions rate of the positive and negative electrolytes resemble the trends of the of the average molar fluxes during charge and discharge. However, considering the average on the whole test, the trend of the positive electrolyte cross-over reactions rate deviates from the behaviour of the other cases. Indeed, the cross-over parasitic current density for the positive electrolyte in Fig. 6F

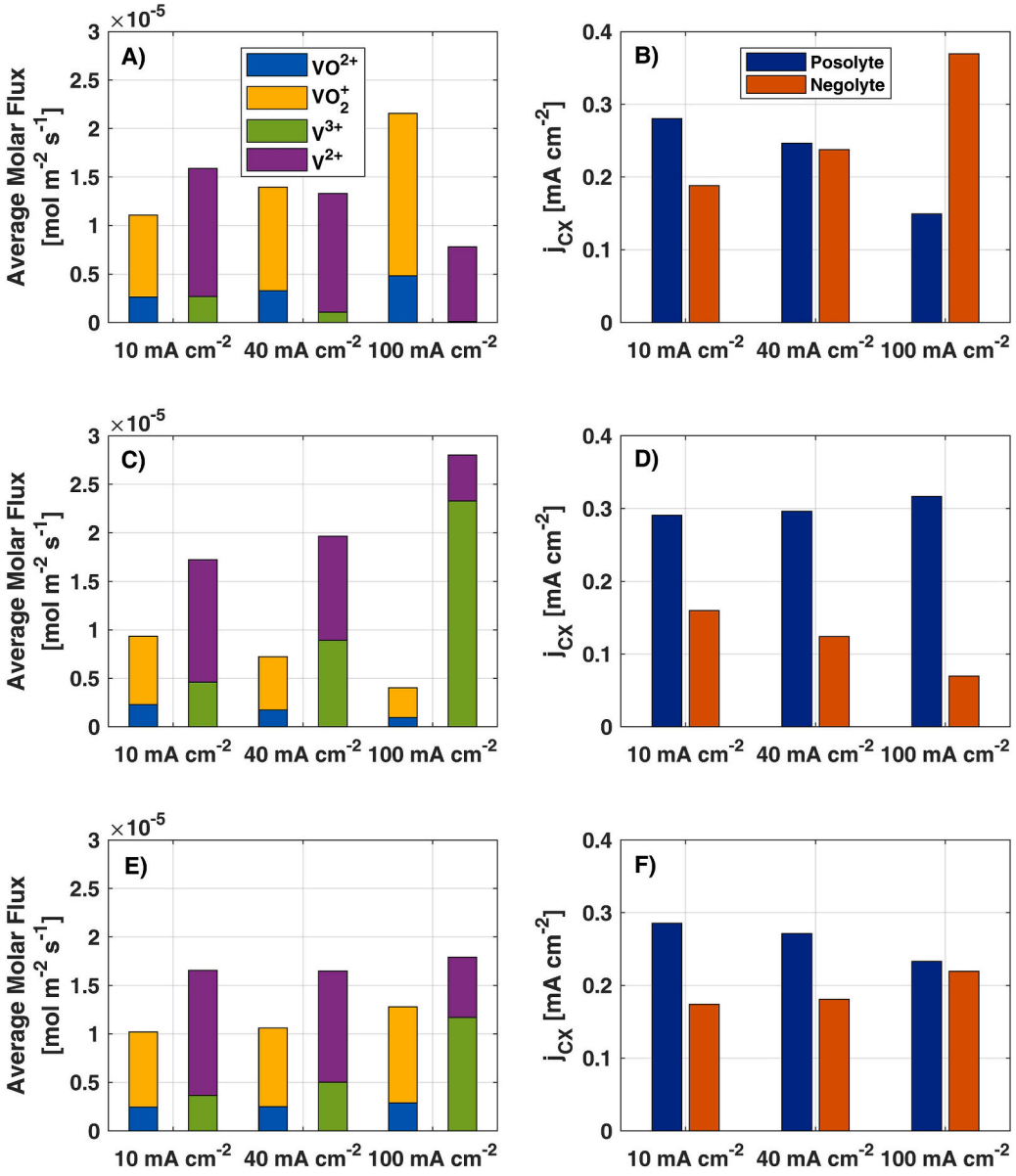


**Fig. 6.** Average cross-over fluxes of the vanadium species A) during charge, C) during discharge and E) cycle average. Average electrolyte solutions cross-over reactions rate B) during charge, D) during discharge and F) cycle average.

decreases (0.29 mA $cm^{-2}$ at 10 mA $cm^{-2}$ to 0.23 mA $cm^{-2}$ at 100 mA $cm^{-2}$) despite increased fluxes from the negative electrolyte (Fig. 6E). This unexpected behaviour is due to the fact that at increasing operating current density the share of $V^{3+}$ on the overall flux increases from 22 % at 10 mA $cm^{-2}$ to 65 % at 100 mA $cm^{-2}$ (Fig. 6E). Thus, considering that $V^{3+}$ is the less harmful species for the positive electrolyte, the rate of the cross-over current at the positive electrolyte decreases. As regards the average self-discharge rate of the negative electrolyte on the whole test, since the flux of $VO_2^+$ is the most predominant flux from the positive electrolyte at each current density (Fig. 6E) the cross-over parasitic current density for the negative electrolyte increases (0.17 mA $cm^{-2}$ at 10 mA $cm^{-2}$ to 0.22 mA $cm^{-2}$ at 100 mA $cm^{-2}$, Fig. 6F) along with increased fluxes of the positive electrolyte (Fig. 6E).

The highlighted behaviours of the cross-over fluxes and cross-over reactions rate of the electrolytes show thus that a higher flux of vanadium cross-over not always leads to a higher self-discharge of the electrolytes due to the different complex mechanisms that interplay in cross-over phenomena. Fig. 6F shows also that at the investigated operating conditions the self-discharge of the positive electrolyte is always higher than the one of the negative electrolyte, coherently with the measurements of the self-discharge of the electrolyte with the RHE reported in Fig. 3B and C.

As stated previously, operating at higher current density allows to reduce the net vanadium transport between the two electrolytes. Moreover, increasing the current density permits to mitigate the self-discharge of the positive electrolyte, which has the highest cross-over parasitic current density at each current density, alleviating thus the most critical self-discharge. Indeed, the results reported in Fig. 3 showed a lower SoC loss per cycle at 100 mA $cm^{-2}$, allowing the battery to operate for a larger number of cycles. Increasing the current density beyond 100 mA $cm^{-2}$ could have triggered side reactions due to the larger over-potentials reached with the employed electrodes. For this reason, the analysis reported in this work is limited to operating current densities up to 100 mA $cm^{-2}$.

Fig. 7 compares the migrative and diffusive average fluxes at the three different current densities during charge and discharge. Since the concentration gradient and potential gradient are not constant in the membrane, the fluxes reported are an average on the thickness of the

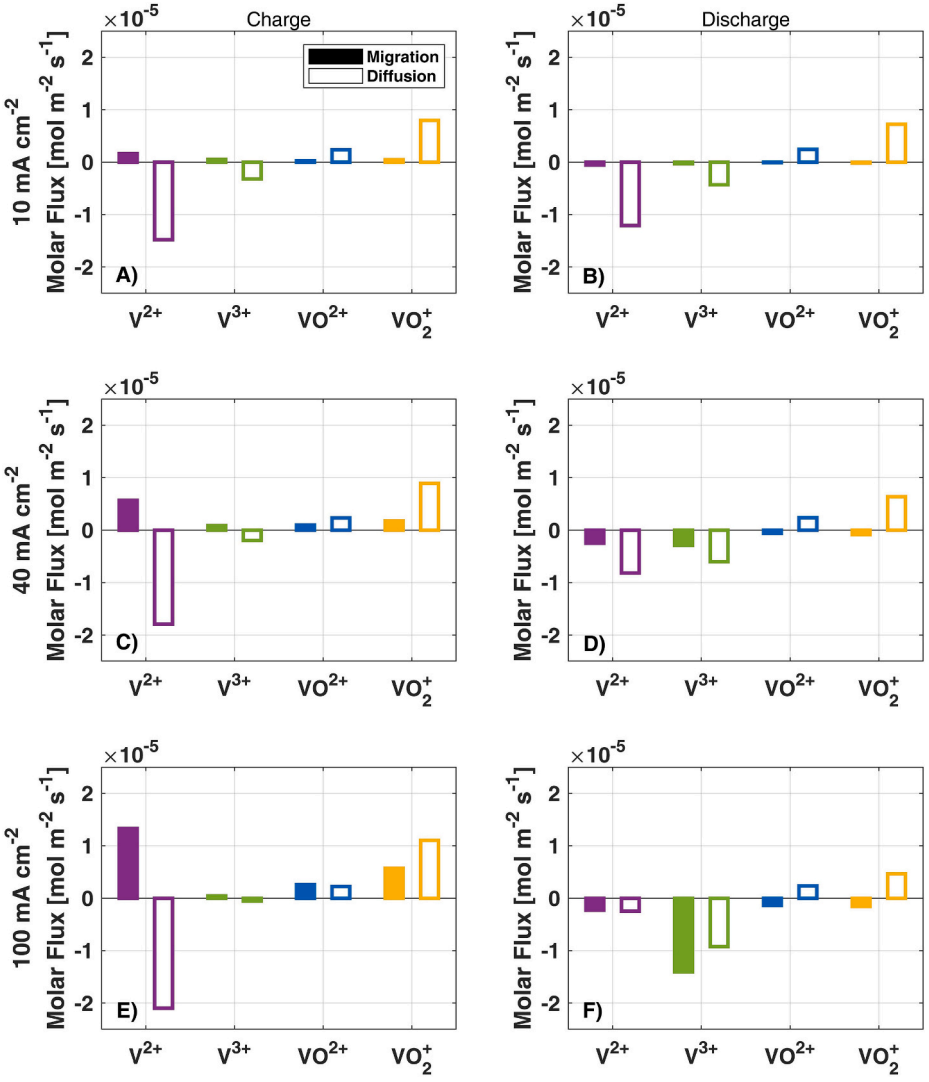


**Fig. 7.** Migrative and diffusive flux through the membrane for the different species at different operating conditions: A, B) 10 mA $cm^{-2}$, C, D) 40 mA $cm^{-2}$ E, F) 100 mA $cm^{-2}$. A,C,E) During charge and B,D,F) during discharge.

membrane. A positive value represents a flux directed from the positive electrolyte to the negative electrolyte, while a negative value the opposite direction. As it can be seen in Fig. 7, during charge the migrative flux is always directed towards the negative electrolyte, while during discharge is towards the positive electrolyte. Moreover, the migrative fluxes increase with the increasing current density, accordingly to the electrolytic potential gradient through the membrane. As regards the diffusive flux, the direction is always towards the opposite electrolyte independently from the current. However, the flux of the charged species, $V^{2+}$ and $VO_2^+$, increases during charge and decrease during discharge, while for discharge species, $V^{3+}$ and $VO^{2+}$, the trend is the opposite. This is due to the fact that during charge the concentration of the charged species at the membrane-electrode interface is higher than the one of the discharged species, while during discharge the discharged species present the higher concentrations at the interface (Fig. S6 of the Supplementary Materials).

After evaluating the intensity of the diffusive and migrative fluxes, it is possible to analyse which is the dominating transport mechanism for cross-over fluxes in the considered operating conditions. Fig. 8 reports the ratio between the diffusive flux and the total flux for the different vanadium species. This ratio is calculated during charge for the positive electrolyte species and during discharge of the negative electrolyte species, i.e. when diffusive and migrative fluxes have the same direction. At lower current densities diffusion is the dominant transport mechanism as its contribution to the overall flux is around 95 % for all species, except for $VO^{2+}$ which is around 90 %. Increasing the current leads to a reduction of the contribution of diffusion as the migrative flux increases and thus diffusion and migration contribute equally to the cross-over with a contribution between 40 % and 66 %.

The proposed modelling analysis showed the intrinsic complexity of the cross-over phenomena and the influence of the current density and migrative flux on cross-over fluxes. In particular, both diffusive and migrative fluxes must be considered in the evaluation of cross-over losses in VRFB during the design of separators and during the definition of operating strategies for the mitigation of battery self-discharge and electrolyte imbalance.

## 5. Conclusions

In this work a new and comprehensive approach for the investigation of cross-over fluxes in VRFB is proposed. This approach is based on the calibration of a 1D physically-based model of the operation of a VRFB on the self-discharge of the singles electrolytes measured via through-plate RHE at different operating conditions during charge-discharge cycles with fixed exchange capacity. The model was calibrated on the results of test on three different current densities, obtaining parameters able to

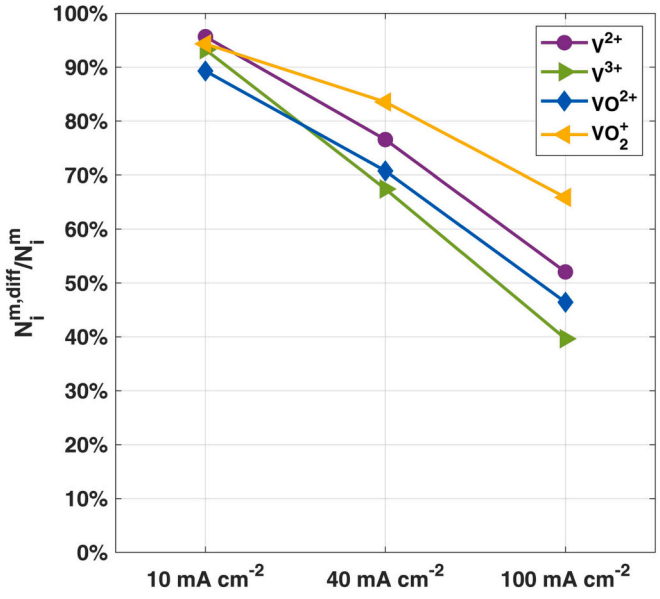


**Fig. 8.** Contribution of the diffusive flux on the overall cross-over flux for the vanadium species.

successfully describe the electrochemistry, the mass transport, the vanadium transport through the membrane and the self-discharge of the electrolyte solutions at different operating conditions. This approach allows to define model parameters with reduced uncertainty compared, increasing the reliability of model predictions.

The main conclusions of the work are the following:

- Comparing at the same number of cycle, a higher operating current density allows to reduce the self-discharge of the battery and the electrolyte imbalance due to vanadium cross-over.

At each current density the positive electrolyte suffers a faster self-discharge than the negative electrolyte due to the higher value of the diffusivities in the membrane for the vanadium ions $V^{2+}$ and $V^{3+}$.

- According to the modelling analysis, the net vanadium transport is towards the positive electrolyte and it decreases as the operating current density increases, reducing by 19 % from 10 mA cm$^{-2}$ to 100 mA cm$^{-2}$.
- Increasing the operating current density, the cross-over reactions rate of the negative electrolyte increases, while it decreases for the positive electrolyte despite increasing fluxes from the negative electrolyte. This is consequence of the fact that the different vanadium species have different effect of the self-discharge of the electrolytes, in particular this behaviour is due to a change in the composition of the net flux, as the flux of $V^{3+}$, the least harmful species for the positive electrolyte, becomes more dominant at higher current densities.
- According to the modelling analysis of the cross-over fluxes, a current density of 100 mA cm$^{-2}$ may be the best operating conditions among the investigated ones as it allows to reduce the net transport of vanadium ions between the two electrolyte and it helps in mitigating the self-discharge of the positive electrolyte, which resulted to be the one most affected by cross-over losses.
- At low current density diffusion is the main mechanism for vanadium transport through the membrane, while at higher current density diffusion and migration contribute almost equally to the vanadium fluxes.

## CRediT authorship contribution statement

**Cecchetti Marco:** Conceptualization, Methodology, Validation, Formal analysis, Investigation, Data curation, Writing – original draft, Visualization. **Toja Francesco:** Methodology, Formal analysis, Investigation, Data curation. **Casalegno Andrea:** Supervision, Project administration. **Zago Matteo:** Conceptualization, Methodology, Resources, Writing – review & editing, Visualization, Supervision, Project administration.

## Declaration of competing interest

The authors declare that they have no known competing financial interests or personal relationships that could have appeared to influence the work reported in this paper.

## Data availability

The data that has been used is confidential.

## Appendix A. Supplementary data

Supplementary data to this article can be found online at https://doi.org/10.1016/j.est.2023.107846.

## References

[1] M. Jafari, A. Botterud, A. Sakti, Decarbonizing power systems: a critical review of the role of energy storage, Renew. Sust. Energ. Rev. 158 (2022), 112077, https://doi.org/10.1016/j.rser.2022.112077.
[2] M. Arbabzadeh, R. Sioshansi, J.X. Johnson, G.A. Keoleian, The role of energy storage in deep decarbonization of electricity production, Nat. Commun. 10 (2019) 3413, https://doi.org/10.1038/s41467-019-11161-5.
[3] T. Bobmann, I. Staffell, The shape of future electricity demand: exploring load curves in 2050s Germany and Britain, Energy. 90 (2015) 1317–1333, https://doi.org/10.1016/j.energy.2015.06.082.
[4] Renewables, International Energy Agency (IEA). https://www.iea.org/reports/renewables-2022, 2022. License: CC BY 4.0.
[5] Grid-Scale Storage, Internation Energy Agency (IEA). https://www.iea.org/reports/grid-scale-storage, 2022. License: CC BY 4.0.
[6] World Energy Investment, International Energy Agency (IEA). https://www.iea.org/reports/world-energy-investment-2022, 2022. License: CC BY 4.0.
[7] E. Sánchez-Díez, E. Ventosa, M. Guarnieri, A. Trovò, C. Flox, R. Marcilla, F. Soavi, P. Mazur, E. Aranzabe, R. Ferret, Redox flow batteries: status and perspective towards sustainable stationary energy storage, J. Power Sources 481 (2021), https://doi.org/10.1016/j.jpowsour.2020.228804.
[8] Inkwood Research, Size of the global battery market from 2018 to 2021, with a forecast through 2030, by technology (in million U.S. dollars)., Statista. https://www.statista.com/statistics/1339880/global-battery-market-size-by-technology/, 2022. (Accessed 26 April 2023).
[9] A. Trovò, F. Picano, M. Guarnieri, Comparison of energy losses in a 9 kW vanadium redox flow battery, J. Power Sources 440 (2019), 227144, https://doi.org/10.1016/j.jpowsour.2019.227144.
[10] Y. Lei, B.W. Zhang, B.F. Bai, T.S. Zhao, A transient electrochemical model incorporating the Donnan effect for all-vanadium redox flow batteries, J. Power Sources 229 (2015) 202–211, https://doi.org/10.1016/j.jpowsour.2015.08.100.
[11] A. Tang, J. Bao, M. Skyllas-Kazacos, Dynamic modelling of the effects of ion diffusion and side reactions on the capacity loss for vanadium redox flow battery, J. Power Sources 196 (2011) 10737–10747, https://doi.org/10.1016/j.jpowsour.2011.09.003.
[12] K.W. Knehr, E. Agar, C.R. Dennison, A.R. Kalidindi, E.C. Kumbur, A transient vanadium flow battery model incorporating vanadium crossover and water transport through the membrane, J. Electrochem. Soc. 159 (2012) A1446–A1459, https://doi.org/10.1149/2.017209jes.
[13] B. Jiang, L. Wu, L. Yu, X. Qiu, J. Xi, A comparative study of Nafion series membranes for vanadium redox flow batteries, J. Membr. Sci. 510 (2016) 18–26, https://doi.org/10.1016/j.memsci.2016.03.007.
[14] V. Viswanathan, A. Crawford, D. Stephenson, S. Kim, W. Wang, B. Li, G. Coffey, E. Thomsen, G. Graff, P. Balducci, M. Kintner-Meyer, V. Sprenkle, Cost and performance model for redox flow batteries, J. Power Sources 247 (2014) 1040–1051, https://doi.org/10.1016/j.jpowsour.2012.12.023.
[15] C. Minke, U. Kunz, T. Turek, Techno-economic assessment of novel vanadium redox flow batteries with large-area cells, J. Power Sources 361 (2017) 105–114, https://doi.org/10.1016/j.jpowsour.2017.06.066.
[16] C. Minke, M.A. Dorantes Ledesma, Impact of cell design and maintenance strategy on life cycle costs of vanadium redox flow batteries, J. Energy Storage. 21 (2019) 571–580, https://doi.org/10.1016/j.est.2018.12.019.

[17] Y. Shi, C. Eze, B. Xiong, W. He, H. Zhang, T.M. Lim, A. Ukil, J. Zhao, Recent development of membrane for vanadium redox flow battery applications: a review, Appl. Energy 238 (2019) 202–224, https://doi.org/10.1016/j.apenergy.2018.12.087.
[18] B.G. Thiam, A. El Magri, S. Vaudreuil, An overview on the progress and development of modified sulfonated polyether ether ketone membranes for vanadium redox flow battery applications, High Perform. Polym. 34 (2022) 131–148, https://doi.org/10.1177/09540083211049317.
[19] S. Won, K. Oh, H. Ju, Numerical analysis of vanadium crossover effects in all-vanadium redox flow batteries.pdf, Electrochim. Acta 177 (2015) 310–320, https://doi.org/10.1016/j.electacta.2015.01.166.
[20] X.G. Yang, Q. Ye, P. Cheng, T.S. Zhao, Effects of the electric field on ion crossover in vanadium redox flow batteries, Appl. Energy 145 (2015) 306–319, https://doi.org/10.1016/j.apenergy.2015.02.038.
[21] Q. Luo, L. Li, Z. Nie, W. Wang, X. Wei, B. Li, B. Chen, Z. Yang, In-situ investigation of vanadium ion transport in redox flow battery, J. Power Sources 218 (2012) 15–20, https://doi.org/10.1016/j.jpowsour.2012.06.066.
[22] L. Hao, Y. Wang, Y. He, Modeling of ion crossover in an all-vanadium redox flow battery with the interfacial effect at membrane/electrode interfaces, J. Electrochem. Soc. 166 (2019) A1310–A1322, https://doi.org/10.1149/2.1061906jes.
[23] J. Shin, B. Jeong, M.F. Chinannai, H. Ju, Mitigation of water and electrolyte imbalance in all-vanadium redox flow batteries, Electrochim. Acta 390 (2021), 138858, https://doi.org/10.1016/j.electacta.2021.138858.
[24] M.Y. Lu, W.W. Yang, Y.M. Deng, W.Z. Li, Q. Xu, Y.L. He, Mitigating capacity decay and improving charge-discharge performance of a vanadium redox flow battery with asymmetric operating conditions, Electrochim. Acta 309 (2019) 283–299, https://doi.org/10.1016/j.electacta.2019.04.032.
[25] Y.A. Gandomi, D.S. Aaron, M.M. Mench, Coupled membrane transport parameters for ionic species in all-vanadium redox flow batteries, Electrochim. Acta 218 (2016) 174–190, https://doi.org/10.1016/j.electacta.2016.09.087.
[26] X.L. Zhou, T.S. Zhao, L. An, Y.K. Zeng, L. Wei, Modeling of ion transport through a porous separator in vanadium redox flow batteries, J. Power Sources 327 (2016) 67–76, https://doi.org/10.1016/J.JPOWSOUR.2016.07.046.
[27] M. Pugach, M. Kondratenko, S. Briola, A. Bischi, Zero dimensional dynamic model of vanadium redox flow battery cell incorporating all modes of vanadium ions crossover, Appl. Energy 226 (2018) 560–569, https://doi.org/10.1016/j.apenergy.2018.05.124.
[28] R.M. Darling, A.Z. Weber, M.C. Tucker, M.L. Perry, The influence of electric field on crossover in redox-flow batteries, J. Electrochem. Soc. 163 (2015) A5014–A5022, https://doi.org/10.1149/2.0031601jes.
[29] P.A. Boettcher, E. Agar, C.R. Dennison, E.C. Kumbur, Modeling of ion crossover in vanadium redox flow batteries: a computationally-efficient lumped parameter approach for extended cycling, J. Electrochem. Soc. 163 (2016) A5244–A5252, https://doi.org/10.1149/2.0311601jes.
[30] K. Oh, M. Moazzam, G. Gwak, H. Ju, Water crossover phenomena in all-vanadium redox flow batteries, Electrochim. Acta 297 (2019) 101–111, https://doi.org/10.1016/j.electacta.2018.11.151.
[31] K. Oh, S. Won, H. Ju, A comparative study of species migration and diffusion mechanisms in all-vanadium redox flow batteries, Electrochim. Acta 181 (2015) 238–247, https://doi.org/10.1016/j.electacta.2015.03.012.
[32] K.W. Knehr, E.C. Kumbur, Role of convection and related effects on species crossover and capacity loss in vanadium redox flow batteries, Electrochem. Commun. 23 (2012) 76–79, https://doi.org/10.1016/j.elecom.2012.07.008.
[33] E. Agar, K.W. Knehr, D. Chen, M.A. Hickner, E.C. Kumbur, Species transport mechanisms governing capacity loss in vanadium flow batteries: comparing Nafion® and sulfonated Radel membranes, Electrochim. Acta 98 (2013) 66–74, https://doi.org/10.1016/j.electacta.2013.03.030.
[34] Y. Lei, B.W. Zhang, B.F. Bai, X. Chen, T.S. Zhao, A transient model for vanadium redox flow batteries with bipolar membranes, J. Power Sources 496 (2021), 229829, https://doi.org/10.1016/j.jpowsour.2021.229829.
[35] Y. Lei, B.W. Zhang, Z.H. Zhang, B.F. Bai, T.S. Zhao, An improved model of ion selective adsorption in membrane and its application in vanadium redox flow batteries, Appl. Energy 215 (2018) 591–601, https://doi.org/10.1016/j.apenergy.2018.02.042.
[36] Y. Wang, L. Hao, Effect of membrane properties on ion crossover in vanadium redox flow batteries, J. Electrochem. Soc. 166 (2019) 3784–3795, https://doi.org/10.1149/2.1011915jes.
[37] C. Lutz, S. Hampel, X. Ke, S. Beuermann, T. Turek, U. Kunz, A. Guilherme Buzanich, M. Radtke, U.E.A. Fittschen, Evidence for redox reactions during vanadium crossover inside the nanoscopic water-body of Nafion 117 using X-ray absorption near edge structure spectroscopy, J. Power Sources 483 (2021), 229176, https://doi.org/10.1016/j.jpowsour.2020.229176.
[38] R.A. Elgammal, Z. Tang, C.N. Sun, J. Lawton, T.A. Zawodzinski, Species uptake and mass transport in membranes for vanadium redox flow batteries, Electrochim. Acta 237 (2017) 1–11, https://doi.org/10.1016/j.electacta.2017.03.131.
[39] J. Xi, Z. Wu, X. Teng, Y. Zhao, L. Chen, X. Qiu, Self-assembled polyelectrolyte multilayer modified Nafion membrane with suppressed vanadium ion crossover for vanadium redox flow batteries, J. Mater. Chem. 18 (2008) 1232–1238, https://doi.org/10.1039/b718526j.
[40] M.W. Verbrugge, R.F. Hill, Ion and solvent transport in ion-exchange membranes: II. A radiotracer study of the sulfuric-acid, Nation-117 system, J. Electrochem. Soc. 137 (1990) 893–899, https://doi.org/10.1149/1.2086574.
[41] C. Sun, J. Chen, H. Zhang, X. Han, Q. Luo, Investigations on transfer of water and vanadium ions across Nafion membrane in an operating vanadium redox flow battery, J. Power Sources 195 (2010) 890–897, https://doi.org/10.1016/j.jpowsour.2009.08.041.
[42] Y.H. Wan, J. Sun, H.R. Jiang, X.Z. Fan, T.S. Zhao, A highly-efficient composite polybenzimidazole membrane for vanadium redox flow battery, J. Power Sources 489 (2021), 229502, https://doi.org/10.1016/j.jpowsour.2021.229502.
[43] I. Derr, A. Fetyan, K. Schutjajew, C. Roth, Electrochemical analysis of the performance loss in all vanadium redox flow batteries using different cut-off voltages, Electrochim. Acta 224 (2017) 9–16, https://doi.org/10.1016/j.electacta.2016.12.043.
[44] I. Derr, M. Bruns, J. Langner, A. Fetyan, J. Melke, C. Roth, Degradation of all-vanadium redox flow batteries (VRFB) investigated by electrochemical impedance and X-ray photoelectron spectroscopy: part 2 electrochemical degradation, J. Power Sources 325 (2016) 351–359, https://doi.org/10.1016/j.jpowsour.2016.06.040.
[45] M. Cecchetti, A. Casalegno, M. Zago, Local potential measurement through reference electrodes in vanadium redox flow batteries: evaluation of overpotentials and electrolytes imbalance, J. Power Sources 400 (2018) 218–224, https://doi.org/10.1016/j.jpowsour.2018.08.033.
[46] P.C. Ghimire, A. Bhattarai, R. Schweiss, G.G. Scherer, N. Wai, Q. Yan, A comprehensive study of electrode compression effects in all vanadium redox flow batteries including locally resolved measurements, Appl. Energy 230 (2018) 974–982, https://doi.org/10.1016/j.apenergy.2018.09.049.
[47] D.S. Aaron, Q. Liu, Z. Tang, G.M. Grim, A.B. Papandrew, A. Turhan, T. A. Zawodzinski, M.M. Mench, Dramatic performance gains in vanadium redox flow batteries through modified cell architecture, J. Power Sources 206 (2012) 450–453, https://doi.org/10.1016/j.jpowsour.2011.12.026.
[48] M. Cecchetti, T.A. Ebaugh, H. Yu, L. Bonville, C. Gambaro, L. Meda, R. Maric, A. Casalegno, M. Zago, Design and development of an innovative barrier layer to mitigate crossover in vanadium redox flow batteries, J. Electrochem. Soc. 167 (2020), 130525, https://doi.org/10.1149/1945-7111/abbbbb.
[49] M. Cecchetti, M. Messaggi, A. Donazzi, A. Facibeni, V. Russo, C.S. Casari, A. L. Bassi, A. Casalegno, M. Zago, A combined morphological and electrochemical characterization of carbon electrodes in vanadium redox flow batteries: insights into positive and negative electrode performance, Electrochim. Acta 329 (2020), 135143, https://doi.org/10.1016/j.electacta.2019.135143.
[50] M. Zago, A. Casalegno, Physically-based impedance modeling of the negative electrode in all-vanadium redox flow batteries: insight into mass transport issues, Electrochim. Acta 248 (2017) 505–517, https://doi.org/10.1016/j.electacta.2017.07.166.
[51] Y. Li, L. Sun, L. Cao, J. Bao, M. Skyllas-Kazacos, Dynamic model based membrane permeability estimation for online SOC imbalances monitoring of vanadium redox flow batteries, J. Energy Storage. 39 (2021), 102688, https://doi.org/10.1016/j.est.2021.102688.
[52] S. Bogdanov, M. Pugach, S. Parsegov, V. Vlasov, F.M. Ibanez, K.J. Stevenson, P. Vorobev, Dynamic modeling of vanadium redox flow batteries: practical approaches, their applications and limitations, J. Energy Storage 57 (2023), 106191, https://doi.org/10.1016/j.est.2022.106191.
[53] A.K. Sharma, C.Y. Ling, E. Birgersson, M. Vynnycky, M. Han, Verified reduction of dimensionality for an all-vanadium redox flow battery model, J. Power Sources 279 (2015) 345–350, https://doi.org/10.1016/j.jpowsour.2015.01.019.
[54] R. Islam, C. Nolen, K. Jeong, Effects of sulfuric acid concentration on volume transfer across ion-exchange membrane in a single-cell vanadium redox flow battery, ASME Int. Mech. Eng. Congr. Expo. 6 (2017) 1–8, https://doi.org/10.1115/IMECE2017-72359.
[55] J.H. Vinco, A.E.E. da C. Domingos, D.C.R. Espinosa, J.A.S. Tenório, M. dos P.G. Baltazar, Unfolding the vanadium redox flow batteries: an indeep perspective on its components and current operation challenges, J. Energy Storage 43 (2021), 103180, https://doi.org/10.1016/j.est.2021.103180.
[56] K. Lourenssen, J. Williams, F. Ahmadpour, R. Clemmer, S. Tasnim, Vanadium redox flow batteries: a comprehensive review, J. Energy Storage 25 (2019), 100844, https://doi.org/10.1016/j.est.2019.100844.
[57] J. Kierzenka, L.F. Shampine, A BVP solver that controls residual and error, J. Numer. Anal. Ind. Appl. Math. 3 (2008) 27–41. https://www.researchgate.net/publication/228748602_A_BVP_solver_that_controls_residual_and_error.
[58] C. Blanc, A. Rufer, Understanding the vanadium redox flow batteries, Paths Sustain. Energy 18 (2) (2010) 334–336, https://doi.org/10.5772/13338.
[59] M. Messaggi, P. Canzi, R. Mereu, A. Baricci, F. Inzoli, A. Casalegno, M. Zago, Analysis of flow field design on vanadium redox flow battery performance: development of 3D computational fluid dynamic model and experimental validation, Appl. Energy 228 (2018) 1057–1070, https://doi.org/10.1016/j.apenergy.2018.06.148.
[60] C. Rabissi, G. Sordi, A. Innocenti, A. Casalegno, Fast and reliable calibration of thermal-physical model of lithium-ion battery: a sensitivity-based method, J. Energy Storage 59 (2023), 106435, https://doi.org/10.1016/j.est.2022.106435.
[61] A.M. Pezeshki, R.L. Sacci, F.M. Delnick, D.S. Aaron, M.M. Mench, Elucidating effects of cell architecture, electrode material, and solution composition on overpotentials in redox flow batteries, Electrochim. Acta 229 (2017) 261–270, https://doi.org/10.1016/j.electacta.2017.01.056.
[62] Q. He, J. Yu, Z. Guo, J. Sun, S. Zhao, T. Zhao, M. Ni, Modeling of vanadium redox flow battery and electrode optimization with different flow fields, E-Prime Adv. Electr. Eng. Electron. Energy 1 (2021), 100001, https://doi.org/10.1016/j.prime.2021.100001.
[63] D. You, H. Zhang, J. Chen, A simple model for the vanadium redox battery, Electrochim. Acta 54 (2009) 6827–6836, https://doi.org/10.1016/j.electacta.2009.06.086.